

UNCLASSIFIED

***Mine Blast Loading:  
Experiments and Simulations***

Charles E. Anderson, Jr.

Thilo Behner

Carl E. Weiss

Sidney Chocron

Rory P. Bigger

Southwest Research Institute®  
P.O. Drawer 28510  
San Antonio, TX 78238

Contract: W56HZV-06-C-0194

SwRI® Report 18.12544/011

***Prepared for:***

US Army RDECOM-TARDEC  
AMSRD-RDTA-RS  
Warren, MI 43897-5000

April 2010

UNCLASSIFIED



UNCLASSIFIED

UNCLASSIFIED



<b>REPORT DOCUMENTATION PAGE</b>				<i>Form Approved</i> <b>OMB No. 0704-0188</b>	
<small>Public reporting burden for this collection of information is estimated to average 1 hour per response, including the time for reviewing instructions, searching data sources, gathering and maintaining the data needed, and completing and reviewing the collection of information. Send comments regarding this burden estimate or any other aspect of this collection of information, including suggestions for reducing this burden to Washington Headquarters Service, Directorate for Information Operations and Reports, 1215 Jefferson Davis Highway, Suite 1204, Arlington, VA 22202-4302, and to the Office of Management and Budget, Paperwork Reduction Project (0704-0188) Washington, DC 20503.</small>					
<b>PLEASE DO NOT RETURN YOUR FORM TO THE ABOVE ADDRESS.</b>					
<b>1. REPORT DATE (DD-MM-YYYY)</b>		<b>2. REPORT TYPE</b>		<b>3. DATES COVERED (From - To)</b>	
		Technical Report		July 2007 – April 2009	
<b>4. TITLE AND SUBTITLE</b>  Mine Blast Loading: Experiments and Simulations				<b>5a. CONTRACT NUMBER</b> W56HZV-06-C-0194	
				<b>5b. GRANT NUMBER</b>	
				<b>5c. PROGRAM ELEMENT NUMBER</b>	
<b>6. AUTHOR(S)</b>  Charles E. Anderson, Jr., Thilo Behner, Carl E. Weiss, Sidney Chocron, Rory P. Bigger				<b>5d. PROJECT NUMBER</b>	
				<b>5e. TASK NUMBER</b>	
				<b>5f. WORK UNIT NUMBER</b>	
<b>7. PERFORMING ORGANIZATION NAME(S) AND ADDRESS(ES)</b> Southwest Research Institute, P.O. Drawer 28510, San Antonio, TX 78238				<b>8. PERFORMING ORGANIZATION REPORT NUMBER</b>  18.12544/011	
<b>9. SPONSORING/MONITORING AGENCY NAME(S) AND ADDRESS(ES)</b>  US Army Tank-Automotive Research, Development, and Engineering Center, Warren, MI 48397-5000				<b>10. SPONSOR/MONITOR'S ACRONYM(S)</b> RDECOM-TARDEC	
				<b>11. SPONSORING/MONITORING AGENCY REPORT NUMBER</b>	
<b>12. DISTRIBUTION AVAILABILITY STATEMENT</b>  Distribution A: Approved for Public Release; distribution is unlimited.					
<b>13. SUPPLEMENTARY NOTES</b> The views, opinion, and/or findings contained in this report are those of the authors and should not be construed as an official Department of the Army position, policy, or decision, unless so designated by other documents.					
<b>14. ABSTRACT</b> A series of mine-blast loading experiments were conducted where the soil moisture content, plate standoff distance, and plate shape (flat and V-shaped) were varied. Three experiments were conducted for each test configuration to quantify repeatability of the experiments. The primary experimental diagnostic was the initial velocity imparted to the plate, as inferred from the maximum height that the plate displaced. Numerical simulations were conducted to examine the ability to reproduce the experimental measurements using the wavecode CTH and a modified soil equation of state (EOS) developed by Kerley. The EOS explicitly accounts for soil moisture content and initial distension (porosity). It was found that the initial soil density was extremely important in reproducing the experimental results. It is shown that the simulations reproduce, within experimental variability, the momentum transferred from the mine blast (loading by the soil and detonation products) for the flat plate experiments as a function of moisture content and plate distance. However, it was found that the simulations overpredicted the momentum transferred to the V-shaped plates by approximately 50%. We investigated the root cause for this discrepancy. The simulations calculate a turbulent-like flow field characterized by small-scale vorticity (eddy structures) that can only be resolved at the resolution of the grid. The absence of viscous dissipative terms (Reynolds stresses) in the momentum and energy equations results in a coarsely resolved flow field that transfers too much energy to the plate. At finer grid resolutions, the mine blast products are less coherent due to the increased vorticity being generated and result in more localized loading on the plate by eddy flow structures. Although this provides better agreement with experimental results, we were not able to refine the computational grid sufficiently to reproduce the experiments.					
<b>15. SUBJECT TERMS</b> mine blast, impulsive loading, soil moisture content, numerical simulations, mine blast loading, sand equation of state, parametric studies					
<b>16. SECURITY CLASSIFICATION OF:</b> Unclassified, Unlimited Distribution			<b>17. LIMITATION OF ABSTRACT</b>  None	<b>18. NUMBER OF PAGES</b>  72	<b>19a. NAME OF RESPONSIBLE PERSON</b> Mr. Rick Rickert
<b>c. REPORT</b> Unlimited	<b>b. ABSTRACT</b> Unlimited	<b>c. THIS PAGE</b> Unlimited			<b>19b. TELEPHONE NUMBER (Include area code)</b> (586) 282-3914

UNCLASSIFIED

## Table of Contents

	Page
1.0 Introduction.....	1
1.1 Literature Review .....	1
1.2 Objective .....	5
2.0 Experimental Setup.....	7
2.1 Initial Design .....	7
2.2 Pretest Simulations .....	7
2.3 Final Test Bed Configuration and Sand Characteristics .....	9
2.4 HE Charge and Initiator .....	11
2.5 Steel Plates .....	12
2.6 Experimental Procedure .....	14
2.7 Instrumentation.....	15
2.8 Experimental Matrix.....	16
3.0 Experimental Results .....	19
3.1 Cable-Pull Potentiometers: Plate Displacement versus Time .....	19
3.2 Error Analysis of Cable-Pull Potentiometer Data .....	23
3.3 Video Camera.....	23
3.4 Cable-Free Accelerometer.....	25
3.5 Analysis of Experimental Results .....	27
4.0 Numerical Simulations.....	33
4.1 Introduction .....	33
4.2 Equation of State for Sand.....	33
4.2.1 Review of Sand EOS in CTH .....	33
4.2.2 Modifications to the EOS for the Current Experiments.....	35
4.3 Strength and Fracture Model .....	36
4.4 Explosive Charge Mass for Simulations .....	37
4.5 Grid Convergence Study .....	37
4.6 Flat Plate Simulations.....	39
4.6.1 2-D Simulations .....	40

## Table of Contents (Cont'd)

	<b>Page</b>
4.6.2 Effect of EOS, Including Initial Density.....	42
4.6.3 Effect of Charge Mass .....	43
4.6.4 Effect of Soil Strength .....	45
4.6.5 3-D Simulations: Effect of Moisture Content.....	46
4.6.6 Summary of Flat-Plate Simulations.....	46
4.7 V-Shaped Plates .....	47
4.7.1 V-Shaped Plate: 3-D Results .....	47
4.7.2 V-Shaped (Conical) Plates: 2-D Results.....	48
4.7.3 V-Shaped Plates: Summary .....	52
4.8 3-D Flat-Plate Simulations Revisited.....	52
5.0 Summary and Conclusions .....	55
6.0 Acknowledgements.....	57
7.0 References .....	59



## List of Figures

	<b>Page</b>
Figure 1. Schematic drawing of experimental setup .....	7
Figure 2. Material plots for pretest simulations to explore effects of boundary conditions.....	8
Figure 3. Plate momentum vs. time for boundary condition study .....	9
Figure 4. Cardboard barrel (on steel support) used for the experiments .....	10
Figure 5. Accumulative mass vs. sieve size for sand used in test bed .....	11
Figure 6. Comp B cylinder (bottom side) with attached booster charge.....	12
Figure 7. Schematic configuration for the flat steel plate experiment, here with 20-cm standoff between the plate bottom and top of the sand (dimension in figure in mm) .....	12
Figure 8. Schematic configuration for the 120° interior angle steel plate experiment, with 25-cm standoff between plate center of gravity and top of sand (dimension in figure in mm) .....	13
Figure 9. Schematic configuration for the 90° interior angle steel plate experiment, with 25-cm standoff between plate center of gravity and top of sand, (dimension in figure in mm) .....	13
Figure 10. From top to bottom row: setup inside the blast laboratory; position of plates before initiation; post-test photographs .....	14
Figure 11. View from the high-speed camera position. The cables from the potentiometers are near the sides of the steel plate; the accelerometer recorder is placed in the middle of the plate .....	16
Figure 12. Example of data from the cable-pull potentiometers .....	19
Figure 13. Potentiometer results for flat plate, 20-cm standoff, 7% moisture .....	20
Figure 14. Potentiometer results for flat plate, 30-cm standoff, 7% moisture .....	20
Figure 15. Potentiometer results for V-shaped (90°) plate, 25-cm standoff, 7% moisture .....	20
Figure 16. Potentiometer results for V-shaped (120°) plate, 25-cm standoff, 7% moisture ....	21
Figure 17. Potentiometer results for flat plate, 20-cm standoff, 14% moisture .....	21

## List of Figures (Cont'd)

	<b>Page</b>
Figure 18. Potentiometer results for flat plate, 20-cm standoff, 21% moisture .....	21
Figure 19. Potential error or uncertainty in jump velocity for measured potentiometer data ..	23
Figure 20. Upward motion of the steel plate for Exp. 14 .....	24
Figure 21. Downward motion of the steel plate for Exp. 14 .....	24
Figure 22. Acceleration-time for Exp. 18.....	25
Figure 23. Expanded scales for the ordinate and abscissa axes of Fig. 22.....	26
Figure 24. Velocity-time for Exp. 18, from time integration of the data in Fig. 22.....	26
Figure 25. Displacement-time for Exp. 18, from time integration of the data in Fig. 24 .....	27
Figure 26. Comparison of calculated jump velocities for flat-plate and V-shaped plate experiments .....	28
Figure 27. Jump velocities with standard errors for flat-plate and V-shaped plate experiments .....	28
Figure 28. Comparison of calculated jump velocities for flat-plate experiments vs. sand moisture content.....	29
Figure 29. Jump velocities with standard errors for flat-plate experiments vs. sand moisture content.....	29
Figure 30. Plate momentum as a function of moisture content (20.0-cm standoff).....	30
Figure 31. Measured sand density as a function of moisture content .....	30
Figure 32. Transferred momentum vs. moisture content (20.0-cm standoff); the overlaid squares show the relation between momentum and sand density.....	31
Figure 33. Pressure vs. density response for 14% moisture content with different initial soil densities (porosities).....	35
Figure 34. Pressure vs. density response for two different moisture contents with same initial density.....	36
Figure 35. Plate momentum vs. grid resolutions: 2-D simulations—20-cm standoff.....	38

**List of Figures (Cont'd)**

	<b>Page</b>
Figure 36. Plate momentum for various grid resolutions: 2-D simulations—30-cm standoff .....	38
Figure 37. Plate momentum for various grid resolutions: 3-D simulations—20-cm standoff .....	39
Figure 38. Material plots of mine blast loading of flat plate at 20-cm standoff.....	40
Figure 39. Pressure contours for mine blast loading of flat plate at 20-cm standoff .....	41
Figure 40. Expanded view of select times after detonation for mine blast loading of flat plate .....	42
Figure 41. Initial soil density vs. moisture content (default values in CTH) .....	43
Figure 42. Plate momentum vs. time for various EOS's.....	43
Figure 43. Effect of HE mass on plate momentum: 20-cm standoff (2-D).....	44
Figure 44. Effect of HE mass on plate momentum: 30-cm standoff (2-D).....	44
Figure 45. Parametric study on strength of soil.....	45
Figure 46. Comparison of 3-D simulation results of flat-plate experiment: jump velocity vs. soil moisture content .....	46
Figure 47. Jump velocity vs. plate type: 3-D simulations and experimental results.....	47
Figure 48. Plate momentum vs. time for V-shaped plates: 3-D simulations.....	48
Figure 49. Plate momentum (90°-conical plate) as a function of treatment of mixed cells .....	49
Figure 50. Plate momentum for 90°-conical plate as a function of zone size (2-D) .....	50
Figure 51. Material plots showing loading of 90° V-shaped conical plate at 1.0 ms.....	51
Figure 52. Plate momentum for 120°-conical plate as a function of zone size .....	52
Figure 53. Effect of HE mass on flat-plate momentum: 20-cm standoff (3-D) .....	53
Figure 54. Effect of HE mass on flat-plate momentum: 30-cm standoff (3-D) .....	53

UNCLASSIFIED

## List of Tables

	<b>Page</b>
Table 1. Sieve Distribution for Sand.....	10
Table 2. Sand Densities for Different Moisture Contents.....	11
Table 3. Estimate of Masses of V-Shaped Plates.....	13
Table 4. Experimental Test Matrix .....	17
Table 5. Experimental Results .....	22
Table 6. Moisture content and initial densities for the different soil models developed by Kerley [33] and implemented into CTH .....	34
Table 7. Number of Zones Resolving Elements of Mine Blast Loading Problem .....	37

UNCLASSIFIED

UNCLASSIFIED

## 1.0 INTRODUCTION

### 1.1 Literature Review

Land mines and improvised explosive devices (IED) represent a considerable threat to light vehicles and personnel. Prior to describing the experiments and simulations of the current study, a review of the literature helps place the current effort in perspective. In general, most of the articles examine the impulse delivered by the mine, but the focus varies from influence of soil type, depth of burial, water content, structural response, measurement techniques, approaches to mitigate mine blast loading, as well as numerical approaches to model the phenomenology.

One of the earliest documented works to examine mine blast over a large range of parameters was conducted by Westine, et al. [1]. Similitude modeling was performed, and then a test matrix devised for experiments as a function of charge mass and aspect ratio, burial depth, and standoff. Impulse plugs were used for the diagnostic. The experimental data were tabulated, and then used to develop a computer program for floor plate response from land mine explosions. One difficulty with the experimental effort, however, is that in order to cover a large parameter space, no repeat experiments were conducted; thus, there is no indication of test-to-test variability.

Laine, et al. [2], used AUTODYN to compute pressures and impulses from mine detonations for different types of burial, using both sand and fully saturated clay. They describe the equation of state used to model the two types of materials. They found that the incident impulse is more focused straight above the mine for buried mines than for surface mines. Further, they found that soil type has little effect on maximum pressure and impulse for surface mines, but plays a significant role on buried mines.

An idealized structural model of a vehicle combined with a closed-form formula for normal pressure impulse was used by Mikhail to study the effect of blast under any location of the vehicle [3]. The total normal impulse for an explosion under the front right wheel was only 48% of the impulse value had it exploded under the center of the vehicle. When the explosion was near the center, there was no significant drop in pressure impulse compared to vehicle center. For an explosion halfway between the front wheel and the vehicle center, the impulse was 86% of the maximum (center-of-vehicle) value.

Zakrisson, et al. [4], performed half-scale experiments and measured structural deformation and impulse transfer from land mines. The authors investigated the influence of moisture content in the sand and depth of burial (0, 50, and 150 mm). They reported that impulse on a flat plate increases with depth of burial (DOB), although there was overlap in total impulse for the 50 and 150-mm DOB experiments. In contrast, plate deformation increased as the DOB was changed from 0 to 50 mm, but then decreased for a DOB of 150 mm. LS-DYNA simulations underestimated measured values, but still described the trend observed in the experiment.

Peles, et al. [5], used the multi-material Euler processor of LS-DYNA to determine the effects of impulse and pressure on a generalized add-on armor structure by measuring dynamic displacement, strain energy, and vertical momentum. The authors varied standoff distance beneath the target, soil type properties, charge's geometric shape (cubic, horizontal cylinder with  $L/D = 2$ , vertical cylinder with  $L/D = 2$ , and sphere), and charge arrangement (buried flush with the surface, surface, and above surface). All these parameters were found to have a significant effect on how the energy is projected onto the plate. Hard, dense soil results in the most damage to the armor. The charge shape influences dispersion and as a result the intensity of pressure and

impulse load applied to the structure. A buried flush charge results in more damage in comparison to a surface charge.

Some studies have focused solely on experimental techniques for quantifying the impulse delivered to a structure. Such techniques could then be used to investigate mitigation approaches for reducing the impulse to the structure. Held, et al. [6], developed an autonomous diagnostic device designed to record the displacement, velocity, and acceleration of the bulge of an RHA steel plate subjected to an anti-tank mine blast. This device was successfully proven on the German mine protection test rig. Skaggs, et al. [7], developed a device for full-scale experiments, called the Vertical Impulse Measurement Fixture (VIMF), to measure impulse to a structure. Nine full-scale experiments were conducted [8] using a saturated sand medium; it was found that the impulse delivered by wet sand was sensitive to standoff distance. Gupta, et al. [9] used CTH 2-D simulations of experiments conducted at the VIMF and calculated impulses for dry sand, wet sand, and clay. They compared results from the simulations to those measured in experiments, but only for clay. Their simulations underpredicted the total impulse, which the authors attribute partially to differences in the boundary conditions.

A number of investigators have used numerical simulations to investigate loading to a structure to assess potential damage and/or mitigation techniques. Cendón, et al. [10], describe the iterative approach that was required to develop protection for an infantry fighting vehicle. They used LS-DYNA—ALE (Arbitrary Lagrangian-Eulerian) for the explosive, soil, and air; Lagrangian for the structure, and the Fluid Structures Interaction module to couple the two—to design and optimize the add-on armor protection. They found that the distance between the landmine and the add-on protection was critical in developing and optimizing appropriate protection.

Colbert, et al. [11], wrote a computer program in Visual Basic that determines if a mine is engaged, and if so, will a lethal interaction occur. The authors provide a basic framework, but only considered a single overburden material and mine type for an example.

Gaudreault, et al. [12], modeled the weld associated heat affected zone (HAZ) of a light armored vehicle against landmines using LS-DYNA. The motivation was to account for the weakening of RHA steel in the HAZ, and its affect on hull fracture. A modified material model was used for the HAZ; the constitutive model was modified to match experimental results for an unprotected vehicle. Although the simulations adequately reproduced the experimental results, the authors note that the material in the HAZ needs to be properly characterized at high strain rates before this approach can be used as a reliable predictive tool.

Hlady, et al. [13], conducted experiments on standard, water-filled, and mine resistant tire inserts (runflat tires) to examine the kinetic energy transferred to a structural test apparatus. The water-filled tires transferred the most kinetic energy to the vehicle, while there was little to no difference between the standard and runflat conditions. The authors also examined the effect of soil type on the kinetic energy transferred, and found that detonations in wet prairie soil transferred five times more kinetic energy to the vehicle than dry sand.

Rolc, et al. [14], used LS-DYNA to compare clamped steel and/or composite plates to loading by the detonation of a buried explosive. Although the authors state that they examined the effects of element type (solid elements and shells), and the effect of computational mesh size, none of these results are described in the article. The composite targets that had the best efficiency (the authors do not explicitly describe how they defined/measured “efficiency”)



against mine explosion consisted of two layers of ARMOX (a type of armor-grade steel) with either balsa or aluminum honeycomb inserted between them.

Several articles have focused on the response of occupants of vehicles and tried to assess potential for injury. Motuz, et al. [15], performed numerical analysis on a simplified lower leg (SLL) model to mimic the response and failure mechanisms of a human leg under the loading conditions of an anti-personnel blast mine. Previous work with the SLL model had considered air blast loading. For mine blast loading, the authors used LS-DYNA to simulate the explosive, soil, air interactions, which were then coupled to the Lagrangian SLL model. The authors compared numerical results for the peak pressure as a function of distance above the soil against experimental data; and they also compared shock front location in gelatin and bone. The authors noted that the numerical simulations predicted reasonable peak pressure arrival times, but the calculated pressures were far too low compared with experimental results. They also noted that distortion of the Lagrangian mesh in the coupled ALE model limited the effective run times to approximately 200  $\mu$ s; whereas the authors estimated that run times on the order of 1.5 ms are necessary to capture relevant SLL model response.

Mikhail [16] analyzed crew member accelerations in a light combat vehicle from three main threats: land mine blast, high-explosive munitions, and large-caliber projectiles. He estimated vehicular acceleration and the resulting acceleration of the crew inside. The author estimated the resulting injuries by use of the articulated total body code to provide body acceleration, and then compared these values to established medical thresholds. Large land mines were a more severe threat for acceleration injuries than blast from nearby bursts of large-caliber HE munitions or impact by a large-caliber KE weapon (assuming no perforation). The accelerations at the pelvic area exceeded limits for total incapacitation, although the accelerations at the head were within limits for the cases studied.

A kinematic analytical model to examine the protection afforded vehicle occupants by various types of foam pillars/panels was developed by Cendón, et al. [17]. They checked the validity of the model by conducting LS-DYNA simulations. The authors found that foam solutions were very effective in protecting an occupant against high accelerations induced by blast, while costing less and weighing less than current dampening systems.

Experiments and simulations have also been used to provide a more fundamental understanding of the coupling of the energy between the explosive and soil, and the subsequent loading of a structure. Taylor, et al. [18], conducted a fundamental experimental study examining the pressure loading on a flat plate by a high-explosive charge buried in saturated sand using very small ( $\sim 1$  g), laboratory-scale explosive charges. Impact of the soil “cap” is followed by impact of crater ejecta as the crater grows. They found that loading can be divided into two phases. The first phase is quite complex, very brief, and acts on a relatively small area of the target, but provides half of the total impulse. The second phase is dominated by processes associated with the excavation of a crater. The pressures on the target are much lower, but they are applied over a longer time (about 10 times longer than the first phase) and a larger area. This second phase provides approximately half the total impulse. The authors note that because of the Richtmyer-Meshkov instability, pressure measurements are not repeatable.

Bouamoul and Toussaint [19] evaluated two numerical methods, Smooth Particle Hydrodynamics (SPH) and Arbitrary Lagrangian Eulerian (ALE), to simulate a mine blast on a flat plate structure. The two methods gave approximately the same vertical displacement profile (bulging) of the steel plate, but the SPH calculation provided a better correlation with the one experiment that was discussed.

Neuberger, et al. [20] examine the response of circular plates to flush buried charges and compare the results to the response from air blast [21]. They developed Pi terms, using replica scaling for all geometrical parameters and the Hopkinson scaling law for blast. Additionally, they compared normalized maximum deflection of the plate from numerical simulations (LS-DYNA) to experiments as a function of scaled distance from the charge. A Mohr-Coulomb model was used to describe the constitutive response of the soil when the ALE solver of LS-DYNA was used. They also used an analytical loading function to improve computational efficiency. The authors note that significant simplification can be achieved by using results of air blast for that of a buried mine, provided appropriate magnification factors are applied.

Several studies are worthy of an expanded synopsis because of the insights provided by the studies. Heider and Klomfass [22] measured the jump velocity of a flat plate (determined from the maximum height that the plate was displaced vertically) at two standoff distances from a buried charge, and then compared results of numerical simulations to the experiments. They discussed formulation of the soil model that they developed based on work in Refs. [23-24], and then showed that numerical results were in reasonable agreement with experiment. The authors then conducted numerical sensitivity studies to evaluate the influence of the assumed compaction curve for the soil, soil strength parameters, different charge burial depths, and different initial densities of the sand on the specific radial momentum distribution. They showed that initial sand density had a considerable effect on the specific radial momentum distribution; but that variation of strength parameters and the compaction curve had minimum effect on the momentum distribution to the plate. They also showed numerically that increasing the burial depth broadened the specific momentum loading on the plate, but decreased the peak value above the mine (the peak specific impulse decreased rapidly with increasing soil overburden). For the levels of burial investigated, total momentum increased the deeper the charge was buried.

Grujicic, et al. [25], used AUTODYN to calculate the size and shape of the crater for explosives detonated at different depths in water-saturated sand. The authors found that computational and experimental results are in reasonable agreement at short post-detonation times, but the agreement was less satisfactory for final size and shape of the crater. They attribute this lack of agreement to inadequacies in the sand constitutive model. The authors show that small adjustments to the model significantly improve agreement between the computed and experimentally determined crater shapes; and thus, they conclude that reliable/accurate constitutive models are necessary for accurate simulation results. In subsequent articles, Grujicic, et al. [26-27], compare simulation results to experiments using an improved constitutive model that incorporated moisture and rate-of-deformation effects on the compaction curve. They compare simulation results to experiments conducted using the VIMF at the Army Research Laboratory and report much better agreement in the impulse loads than for the original compaction model.

Deshpande, et al. [28], developed a one-dimensional constitutive model using mono-sized spherical particles to understand soil loading of a structure from a mine blast. The constitutive model accounted for two regimes: 1) when the particles are widely dispersed so that contact between particles are treated as collisions, and 2) when packing density is high and contacts are semi-permanent and consolidation is dominated by particle deformation and inter-particle friction. The authors report that classical soil mechanics, such as a Drucker-Prager model, is applicable for the second regime. They show that the momentum transferred to a structure is strongly dependent on initial density for the second regime. Additionally, they examined the spherical expansion of a shell of dry and water-saturated sand, and predicted that dry sand fully

disperses while wet sand will form clumps; and that this clumping exerts higher pressures on nearby structures compared to equivalent dry sand explosions.

Kerley developed tabular equations of state (EOS) for dry and wet sand [29], to support work on the vertical impulse measurement facility (VIMF) [7-8]. He took an EOS table developed for fused quartz, together with the  $p$ - $\alpha$  model [30], to model dry sand. Next, using this table and an existing model for water, he constructed a new EOS table for wet sand. He then conducted calculations in 2-D and 3-D for varying zone sizes for both dry and wet sand. He found that wet sand produced three times more momentum to a plate than dry sand, considerably higher than earlier calculations with other soil models [31-32].

In a subsequent report [33], Kerley generalized the EOS for sand to other soil types, such as clay and alluvium (a soil-silt-clay mixture). He noted that a major difference between sand and clay is that when water is added to sand, it fills the pores, thereby increasing the density. For clays, water can be absorbed into the grains or on particle surfaces; these solid-water interactions can produce swelling, which typically results in a density decrease compared to the dry material. He developed a three-component EOS model: 1) tabular EOS for the solid-water mixture after all voids have been compacted; 2) the  $p$ - $\alpha$  model to describe the compaction of pores in dry and partially saturated materials (the  $p$ - $\alpha$  model is also used to describe swelling behavior, when it exists); and 3) the CTH geological model to compute material strength behavior. Specifically, Kerley described models for concrete sand (lowest water content and highest porosity; highest pore compaction pressure and material strength); clayey sand (intermediate water content and porosity; low pore compaction pressure and material strength); and gravelly clay (highest water content and lowest porosity; low pore compaction pressure and negligible material strength). Sensitivity studies showed that while results are sensitive to the initial porosity of the soil, they were not sensitive to details of the pore compaction. A sensitivity study on material strength showed that momentum transferred to the plate increased significantly as strength of the soil material decreased.

## 1.2 Objective

The objective of this study is to validate the ability of numerical simulations to replicate the loading of a structure to mine blast. Deficiencies of previous studies with respect to validation include complicated structures, limited variation of experimental test conditions, and no quantification of test repeatability (that is, test-to-test variation). Thus, the first part of this effort involved defining and then conducting a series of well-characterized experiments using a relatively simple structure to address the specific limitations of many of the previous studies. Then, numerical simulations of the experiments were performed and results compared to the experiments. Observations and difficulties are highlighted.

UNCLASSIFIED

## 2.0 Experimental Setup

### 2.1 Initial Design

Test setup consisted of a flat plate placed above soil (sand) with a buried high-explosive (HE) charge, simulating a nominal landmine configuration. When the HE charge is initiated and detonates, the plate is loaded by the sand and explosive products. The plate moves upward to a maximum height before falling due to gravitational forces. Measurement of that height allows for a determination of the momentum transferred to the plate by the HE and sand. This setup is similar to experiments described in Ref. [22].

The baseline configuration is shown in Fig. 1. A 300-kg steel plate (80 cm x 80 cm x 6 cm) was placed 20 cm above the top of the soil. The top of the HE was 5.0 cm below the top of the soil. The bare, cylindrical HE charge was 625 grams of Comp B, with a height-to-diameter ratio of 1/3. The positioning of the HE was the same for all tests.

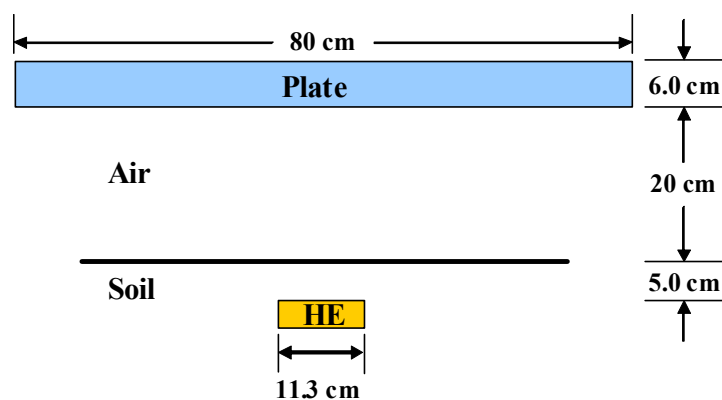


Figure 1. Schematic drawing of experimental setup.

### 2.2 Pretest Simulations

Preparing the soil test bed prior to each experiment can be a very time consuming and expensive process. Thus, it is desirable to limit the amount of soil that has to be prepared for each test. On the other hand, it is desirable to have the test replicate a nominal landmine scenario; i.e., there should be minimal influence of boundaries. It was decided to use numerical simulations to explore the effects of boundary conditions to support final experiment design.

CTH [34] was used to conduct a parameter study on boundary conditions. A soil model, implemented by Kerley [29,33] into CTH, was used for the simulations. Four simulations were conducted; the simulations were run using the 2-D cylindrically symmetry option in CTH. The simulations were:

1. Baseline: 260-cm diameter, 200-cm deep test bed (with transmitting boundaries);
2. 60-cm diameter, 100-cm deep with 5-cm thick steel confinement around the circumference and on the bottom (the 60-cm-diameter, 100-cm-deep dimensions replicated the dimensions used in Ref. [22]);

3. 90-cm diameter, 150-cm deep with 5-cm thick steel confinement around the circumference and on the bottom (1.5 times wider and deeper than simulation #2);
4. 60-cm diameter, 100-cm deep test bed (no confinement, but reflective boundary at the bottom).

The geometries for the simulations, all to the same scale, are shown in Fig. 2. The light blue color denotes air. The white color is outside the computational domain.

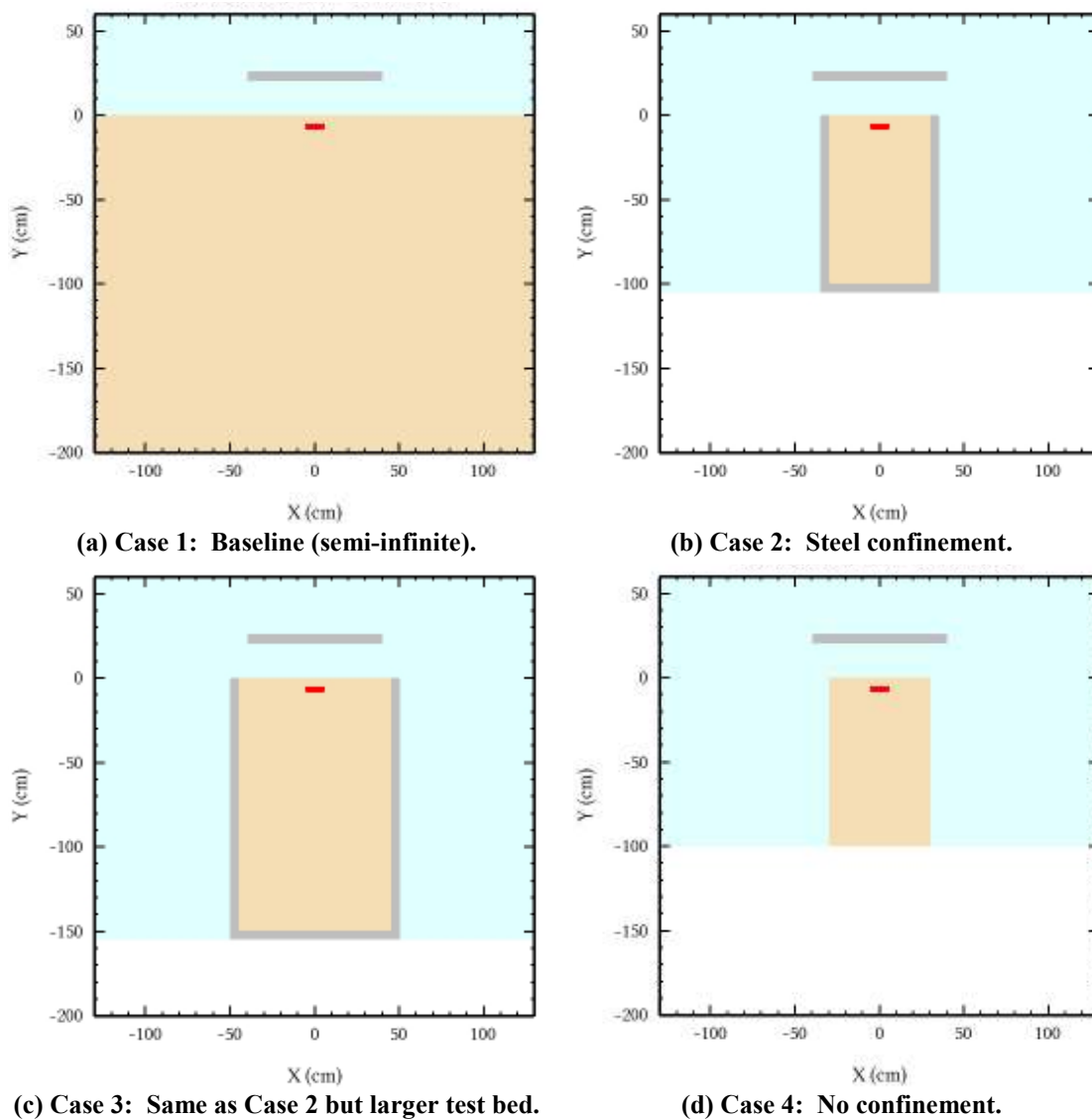


**Figure 2. Material plots for pretest simulations to explore effects of boundary conditions.**

In all cases, the steel plate was 80 cm in diameter (6-cm thick)<sup>1</sup>, 20 cm above the top of the soil test bed, with 625 g of Comp B at 5 cm below the top of the soil (see Fig. 1). The HE is initiated bottom center in the simulations. Note that the plate extends beyond the soil test bed in

<sup>1</sup> There was no attempt at this point to duplicate the mass of the square plate since these were parametric computations to explore the effects of boundary conditions.

Case 2 and Case 4; therefore, these simulations also provide information about plate loading for a finite-width test bed versus a semi-infinite test bed (Case 1).

The plate momentum as a function of time is shown in Fig. 3. It is seen that for approximately the first millisecond, the response of the plate is virtually identical for all the cases. By approximately 1.2 ms, the results for Case 2 diverge from the other results, and in particular, that of the baseline Case 1. Examination of the simulation results for Case 2 show that the pressure wave from detonation of the HE reflects off the bottom and is then collimated by the steel confinement. Additional soil is thrown upward and strikes the plate, increasing the impulse. With the steel boundaries further away—Case 3—this collimation effect is greatly diminished. Lastly, the results for Case 4, which has no confinement, essentially overlay the results of Case 1. It can be seen in the simulations that the pressure wave reflects off the bottom of Case 4, but the radial motion of the soil at the top of the test bed results in rarefaction waves that dissipate the reflected pressure wave.

Since the results for Case 4 are essentially the same as for the baseline Case 1, it was concluded that the Case 4 plate and test bed are sufficiently large to replicate a semi-infinite test bed. The simulations show that bottom-centered detonation of the HE propels the soil mostly vertically, and it is the center of the plate that receives the loading; thus, the radial dimensions of the plate are adequate. In summary, the results of these simulations demonstrated that a semi-infinite test bed can be approximated quite well with a finite test bed using a relatively frangible container to hold the soil. These results were used as input for the final design.

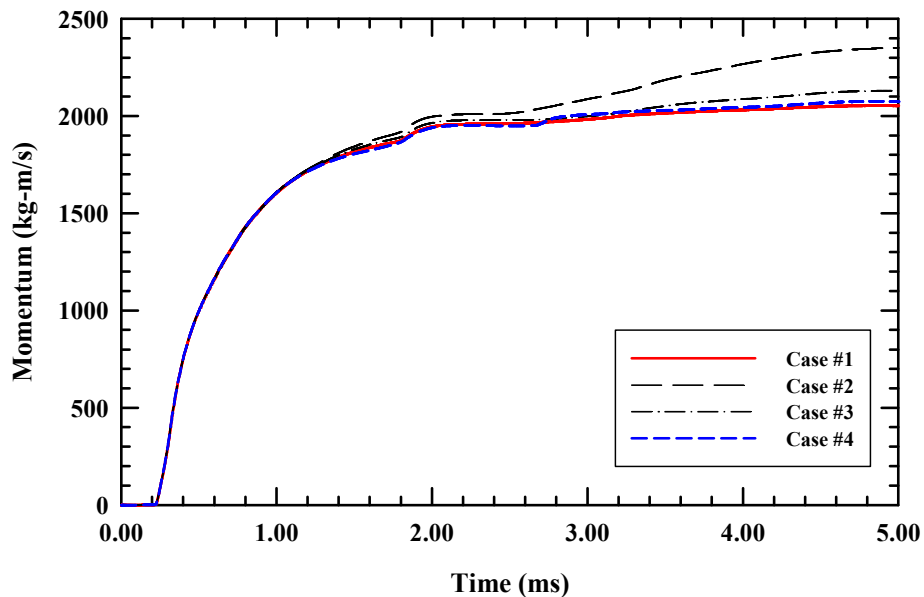


Figure 3. Plate momentum vs. time for boundary condition study.

### 2.3 Final Test Bed Configuration and Sand Characteristics

It was suggested by one of the authors (C. Weiss) that the test bed could be contained in a Sonotube, a round cardboard tube often used as a concrete form. These are quite inexpensive, and thus can be replaced after each test. The cardboard barrel selected had slightly different dimensions than the simulations, but the dimensions were close to those of Case 4, so there was no need to modify the as-delivered barrel. The barrel selected had a height of 85 cm and a

diameter of 63 cm, with a wall thickness of 3 mm. The barrel had a plywood bottom, and both top and bottom were reinforced with a steel ring (Fig. 4). The nominal volume was 255 liters.



**Figure 4. Cardboard barrel (on steel support) used for the experiments.**

The “soil” used for the experiments was standard silica sand with a grain size of up to 1 mm. A sieve system was used to measure the grain distribution; results are shown in Table 1 for two samples. Over 99 % of the sand mass had a grain size less than 0.5 mm. The mass distribution results of Table 1 are plotted in Fig. 5.

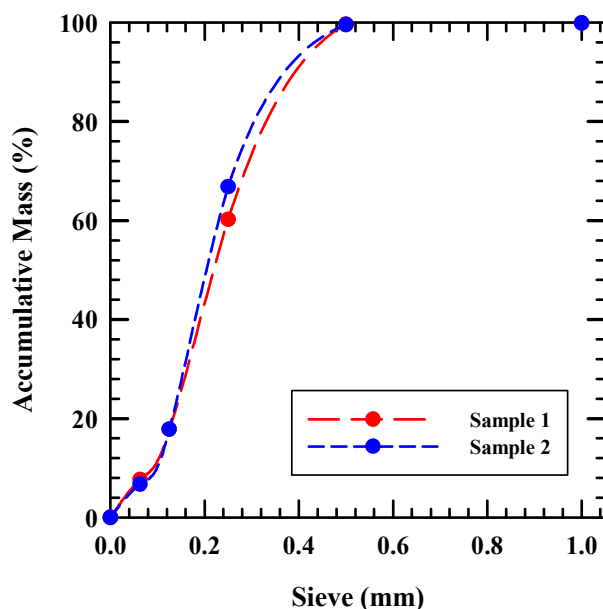
**Table 1. Sieve Distribution for Sand**

<b>Sieve (<math>\mu\text{m}</math>)</b>	<b>Sample 1 mass (g)</b>	<b>Mass (%)</b>	<b>Pass Through (%)</b>
1000	1.0	0.10	99.90
500	2.6	0.26	99.64
250	394	39.40	60.24
125	424	42.40	17.83
63	101.6	10.16	7.67
<63	76.9	7.67	
Sum	999.1	100.00	

<b>Sieve (<math>\mu\text{m}</math>)</b>	<b>Sample 2 mass (g)</b>	<b>Mass (%)</b>	<b>Pass Through (%)</b>
1000	1.2	0.12	99.88
500	3.0	0.30	99.58
250	326.9	32.73	66.85
125	489.4	49.00	17.84
63	111	11.11	6.73
<63	67.2	6.73	
Sum	998.7	100.00	





**Figure 5. Accumulative mass vs. sieve size for sand used in test bed.**

Different moisture contents of the sand were used for the experimental series. The moisture content of a sand sample is defined as the weight of the contained water in the sample divided by the weight of the completely dry sand. Densities of the sand vary with the amount of added water and the grade of compaction. Measurement for the completely sand-filled barrel gave a density value of  $1.37 \text{ g/cm}^3$  with a moisture content of 7% (as delivered). Measurements with a laboratory scale gave the following sand densities as a function of water content, Table 2.

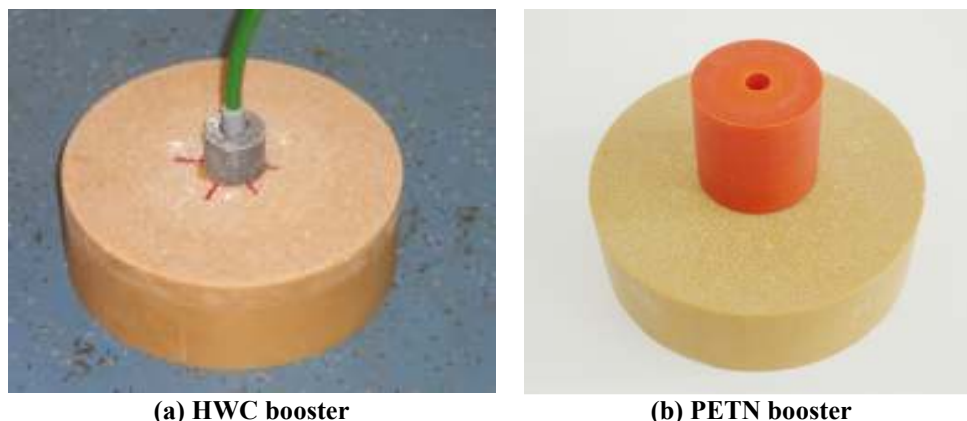
**Table 2. Sand Densities for Different Moisture Contents**

Moisture content (%)	Mean density ( $\text{g/cm}^3$ )
7	$1.37 \pm 0.03$
14	$1.49 \pm 0.03$
22	$1.67 \pm 0.03$

## 2.4 HE Charge and Initiator

The charge used for the experiments was 625 grams of Comp B (density  $\approx 1.7 \text{ g/cm}^3$ ) in cylindrical shape with a height of 3.7 cm and a diameter of 11.3 cm (height-to-diameter ratio of 1/3). The charge was initiated with a booster charge of 8-g HWC and a detonating cord (with attached detonator) for the first three experiments (Fig 6a). This was changed for the remaining experiments to a 10-g PETN booster (inside a plastic cylinder, Fig. 6b) with attached detonator to correct ignition failure, which could occur with the HWC set up.

The charge was placed 5 cm below the top of the sand with the booster charge on the bottom (centered) side. The detonating cord and the detonator wires were guided through a small rubber hose to the side of the barrel prior to filling the cardboard barrel with sand. A placeholder made of Styrofoam was positioned in the sand during the fill of the barrel so that the cavity for the charge was in place for final positioning of the HE.



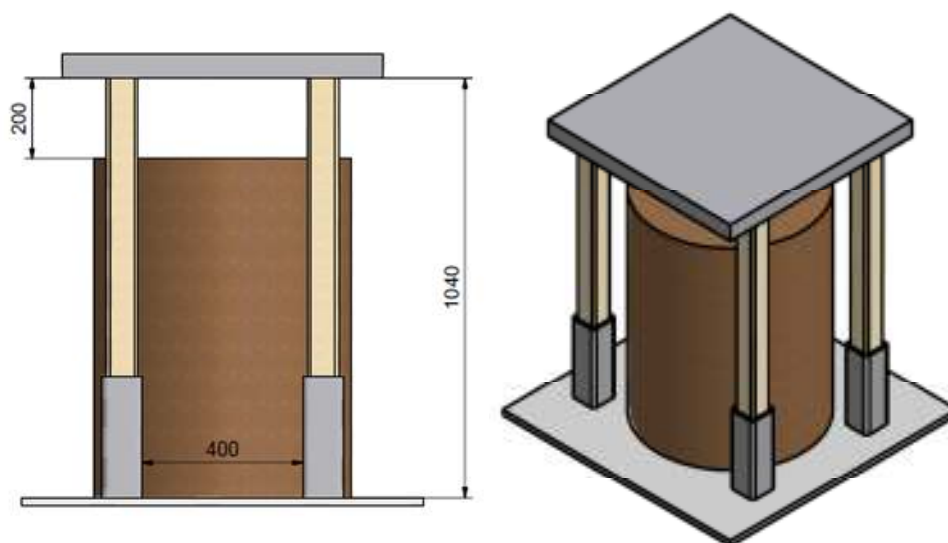
(a) HWC booster

(b) PETN booster

**Figure 6. Comp B cylinder (bottom side) with attached booster charge.**

## 2.5 Steel Plates

The steel plates used in the experiments were either flat or V-shaped with interior angles of  $120^\circ$  or  $90^\circ$ . The flat plate was 80.0 cm x 80.0 cm, and 6.0-cm thick; the weight was 300 kg. Figure 7 shows how the steel plate was positioned above the sand-filled barrel. Wooden poles were cut to the desired length and placed in a steel (angle-iron) support. Lifting rings were mounted on the steel plates, which made it straightforward to move and position the plates.

**Figure 7. Schematic configuration for the flat steel plate experiment, here with 20-cm standoff between the plate bottom and top of the sand (dimension in figure in mm).**

To construct the V-shaped plate, a flat plate was cut in half and butt-welded together. Three small bracing plates were attached at the center of gravity, which also served as mount for the instrumentation used. For the V-shaped plates, some mass was lost in the cutting, but the welds added weight. Additionally, the bracing plates also added weight. The bracing plates were included to preclude the plates deforming inward and breaking the butt weld. Estimates were made of the revised weight using CAD software and weighing the reinforcing plates, as summarized in Table 3. The V-shaped plates had approximately 3% more mass than the flat plate.

**Table 3. Estimate of Masses of V-Shaped Plates**

	V-shaped: 120° interior angle	V-shaped: 90° interior angle
Plate (kg)	150.712 x 2	150.682 x 2
Stiffeners (kg)	2.664 x 3	2.328 x 3
Total Mass (kg)	309.4	308.4
Increase in Weight vs. Flat Plate (%)	3.1	2.8

Figures 8 and 9 depict the positioning of the V-shaped plates above the soil test bed. The center of mass of the plates was positioned 25.0 cm above the top of the test bed.

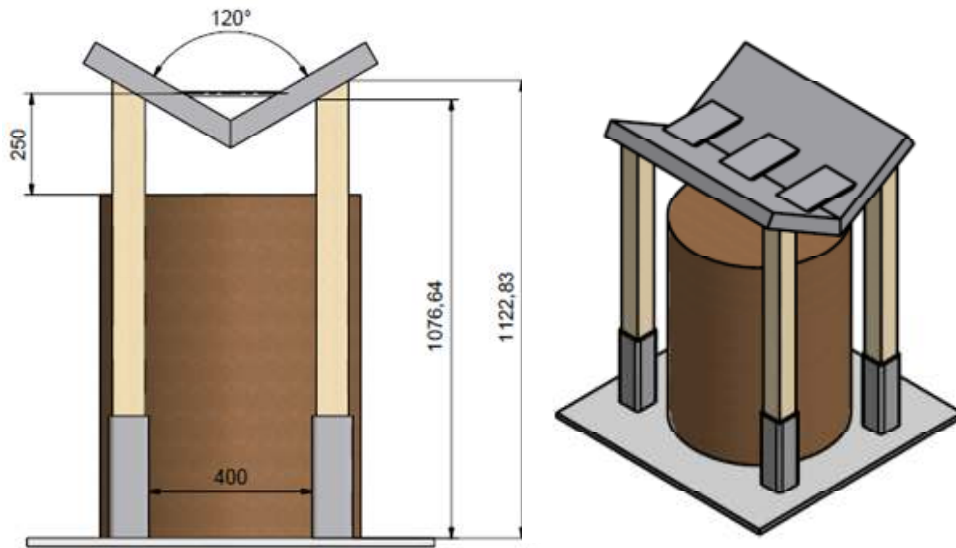


**Figure 8. Schematic configuration for the 120° interior angle steel plate experiment, with 25-cm standoff between plate center of gravity and top of sand (dimension in figure in mm).**

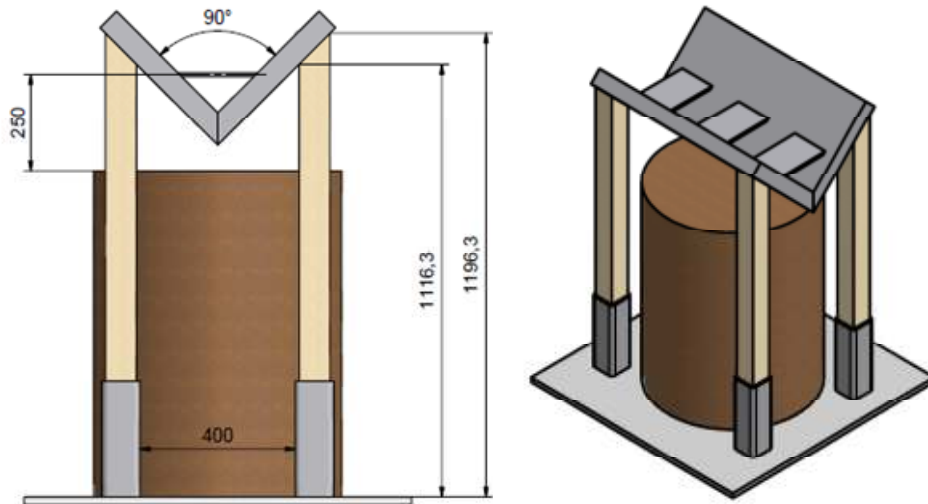


**Figure 9. Schematic configuration for the 90° interior angle steel plate experiment, with 25-cm standoff between plate center of gravity and top of sand (dimension in figure in mm).**

## 2.6 Experimental Procedure

The experiments were performed in the blast laboratory at EMI-Holzen. The steel support was lowered into a concrete recess 2 m by 2 m and 0.75-m deep (Fig. 10). On the bottom of the recess were particle boards, on which the steel support was placed. The charge (in the sand) and the steel plate were well above floor level. After an experiment, only the barrel and the wooden poles had to be replaced.



**Figure 10.** From top to bottom row: setup inside the blast laboratory; position of plates before initiation; post-test photographs.

## 2.7 Instrumentation

It had been decided that the primary diagnostic would be the plate “jump” velocity, that is, the initial velocity of the plate resulting from the impulsive load caused by the stagnating pressure from the sand and blast. This jump velocity,  $V_j$ , can easily be calculated from the maximum height,  $H$ , that the plate moves:

$$V_j = \sqrt{2gH} \quad (1)$$

where  $g$  is the gravitational constant ( $9.8 \text{ m/s}^2$ ). The jump velocity is useful in analysis of structural response where it is assumed that the structure instantaneously has been given an initial velocity  $V_j$ . This assumption will be validated in Section 4.6.

Plate displacement versus time was measured with two cable-pull potentiometers. These were mounted at the ceiling of the blast laboratory and attached to the steel plate centerline (see Fig. 11), so that the cables were extracted before an experiment started and retracted while the steel plate gained height due to detonation of a charge. Once the steel plate reached its maximum height, the cables extracted again during plate descent. The cable-pull potentiometers have a measurement range of 750 cm with a linearity of  $\pm 1.13 \text{ cm}$ . Linearity is defined as the maximum deviation between an ideal straight-line characteristic and the real characteristic of the sensor (without cable slack).

Plate displacement versus time was also monitored with a high-speed video camera. The initial intention was to record the displacement with cameras from two view angles normal to the plate and to each other. However, the specific set-up of the experiments, with the sand in a barrel and the barrel placed in a sinkhole, produced enough sand dust during detonation of the charge to affect visibility of the steel plate from one of the camera positions. It was therefore decided to abandon the two-camera set-up after a few experiments and continue to record the plate displacement with one camera only.

To measure acceleration of the plate directly, a cable-free acceleration recorder was also mounted on top of the steel plate. An acceleration recording is very desirable as it directly gives acceleration history of the plate. Time integration of the acceleration gives the velocity-time history, and integration again gives the displacement-time history. A check on the validity of the acceleration recording is that the total displacement be the same as measured by other instruments. Experience has shown, however, that acceleration histories are difficult to obtain. The initial shock often “overloads” the sensing device, giving bad data and/or resulting in “zero shifts” such that integration of the acceleration data gives numbers that are clearly inconsistent with other data.

The acceleration recorder that was deployed in the experiments had been used successfully in a similar test series where it was mounted on a hull structure; in those experiments, the hull structure dampened the initial shock. In the experiments here, the initial shock delivered to the plate resulted in sensor/recorder malfunction. The recorder could therefore not be used on every test because of repair time; however, the revised (“shock hardened”) recorder functioned properly on the last experiment.

In summary, the main source of data output was the cable-pull potentiometers, which delivered reliable data throughout the experimental series. Optical (high-speed camera) recordings verified the measurements from the potentiometers and provided information about possible plate tilt during an experiment. An acceleration recorder functioned on the last experiment.





**Figure 11. View from the high-speed camera position. The cables from the potentiometers are near the sides of the steel plate; the accelerometer recorder is placed in the middle of the plate.**

## **2.8 Experimental Matrix**

The experimental test matrix was designed with two primary objectives: 1) establish a baseline configuration that allowed a parametric investigation of important variables, and 2) conduct repeat tests to establish test-to-test variability. The baseline condition was described in Fig. 1, a flat plate positioned 20 cm above the sand test bed. The moisture content of the sand was to be the “as-delivered” sand, nominally 6%. From the baseline, the following parametric studies were conducted:

- plate distance
- plate shape
- moisture content.

Three tests were conducted at each condition to establish an estimate of test-to-test variability.

The experimental matrix is summarized in Table 4, which lists the moisture content of the sand, type of plate, and plate distance to the top of the sand. It should be noted that, for the flat plates, distance is measured from the top of the sand to the bottom of the plate while, for the V-shaped plates, distance is measured from the top of the sand to the center of gravity of the plate (as illustrated in Figs. 7 to 9).

Nominal moisture content was planned to be 6, 12 and 18% by mass. Deviation from the desired values occurred in practice (e.g., moisture content of the as-delivered was approximately 7%). Water was added to the sand to increase the moisture content; the moisture content was then measured. The density, as a function of moisture content, was summarized in Table 2.

**Table 4. Experimental Test Matrix**

<b>Test Series</b>	<b>Nominal Moisture Content: Planned (%)</b>	<b>Nominal Moisture Content: Actual (%)</b>	<b>Plate Type</b>	<b>Plate Distance (cm)</b>
1	6	7	Flat	20
2	6	7	Flat	30
3	6	7	V-shape: 90°	25
4	6	7	V-shape: 120°	25
5	12	14	Flat	20
6	18	22	Flat	20

UNCLASSIFIED



### 3.0 Experimental Results

#### 3.1 Cable-Pull Potentiometers: Plate Displacement versus Time

An example of the cable-pull potentiometer data is shown in Fig. 12. The long dashed horizontal line, i.e., the zero line, represents the initial position of the plate as it is supported in place by the wooden pillars (see Figs. 7 and 10). The plate falls below this zero line on descent, falling into the concrete recess, as shown in the bottom row of photographs in Fig. 10. The upward movement of the plate is too fast for the retracting cables, so there can be some cable slack during that motion, as shown with the callout in Fig. 12. After the plate reaches its maximum height, the cable-pull potentiometers record the fall without visible distortion (Fig. 12), i.e., the cables deploy very smoothly. Additionally, although not shown in Fig. 12 (but will be seen in some of the other figures), there is high-frequency noise at very early time that results from the initial shock ringing in the cables and potentiometer housing (this high-frequency noise has dissipated by  $\sim 500 \mu\text{s}$ ).

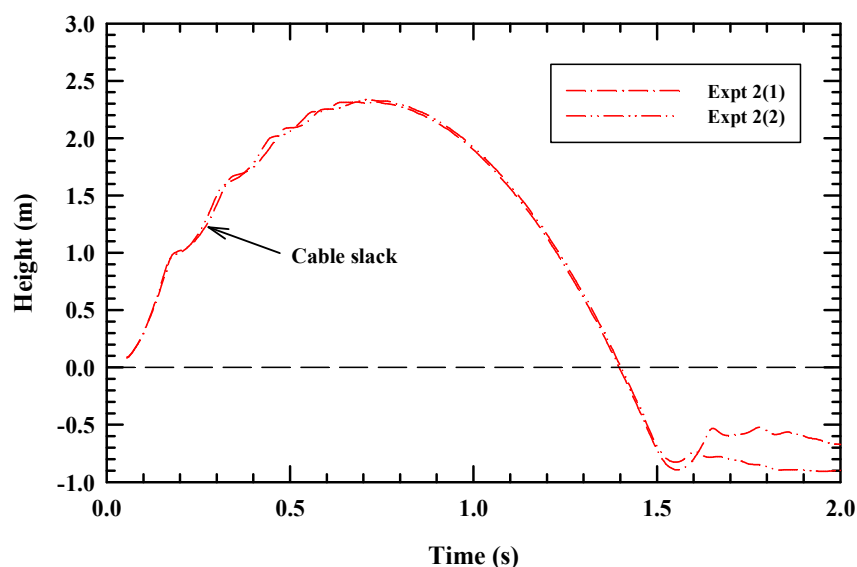


**Figure 12. Example of data from the cable-pull potentiometers.**

Plots of the cable-pull potentiometer results are shown in Figs. 13 through 18. The data are truncated after the plate falls to the “zero” position. All readings were filtered with a 100 Hz low-pass filter using a Bessel function of 2<sup>nd</sup> order (DIAdem analysis software). This eliminates peaks when differentiated to obtain the plate velocity. The first six experiments had an interference signal at the time of ignition (displacement peak),<sup>2</sup> which was blocked by a filter for the remaining experiments. There are several things to notice in the figures. Both potentiometers provided data for all the experiments except for one malfunction on Exp. 3 (Fig. 13). In general, there is excellent agreement between the two potentiometers; as shown in Fig. 12, but there were occasions where the plate was launched upwards with a tilt. Plate tilt was verified by high-speed video coverage (discussed in the next subsection). The largest tilt during

<sup>2</sup> The interference signal was eliminated from Figs. 13 and 14, although some of the effects of the interference signal are seen in the data traces in Fig. 14.

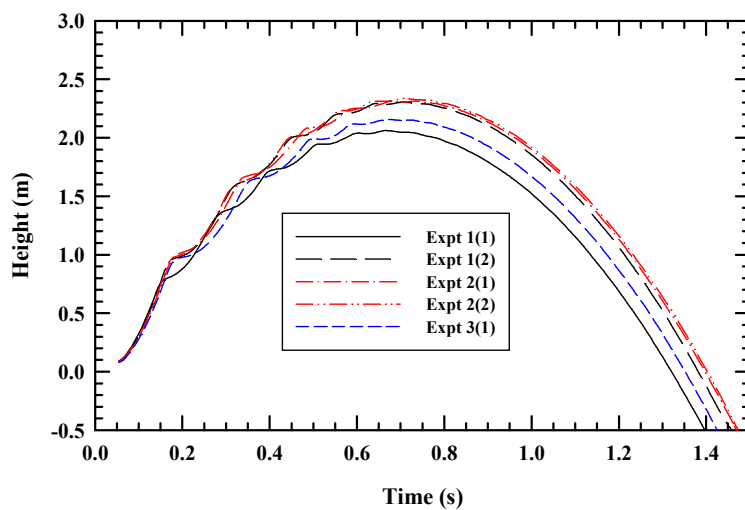


Figure 13. Potentiometer results for flat plate, 20-cm standoff, 7% moisture.

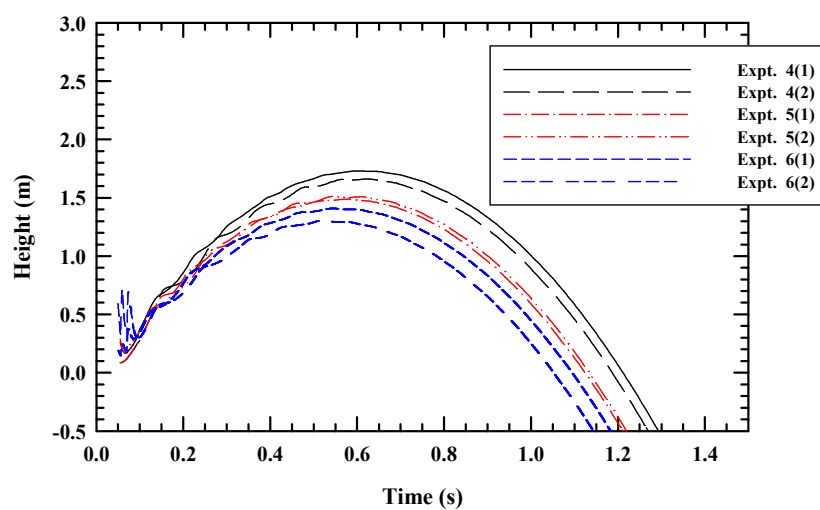


Figure 14. Potentiometer results for flat plate, 30-cm standoff, 7% moisture.

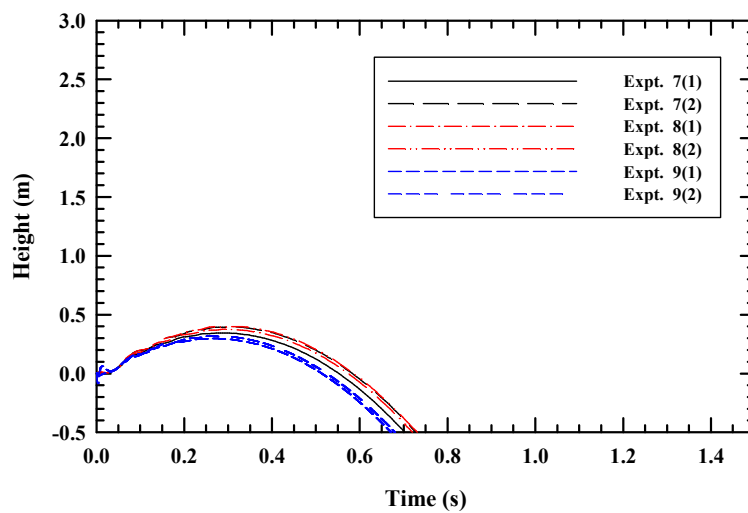


Figure 15. Potentiometer results for V-shaped (90°) plate, 25-cm standoff, 7% moisture.

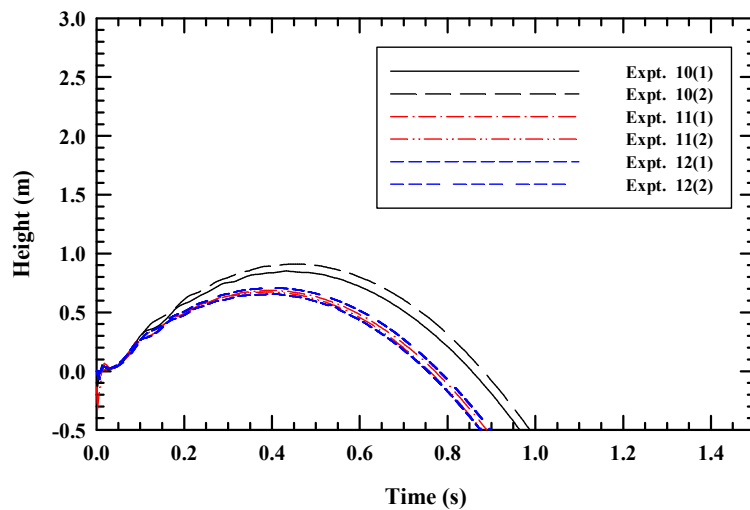


Figure 16. Potentiometer results for V-shaped ( $120^\circ$ ) plate, 25-cm standoff, 7% moisture.

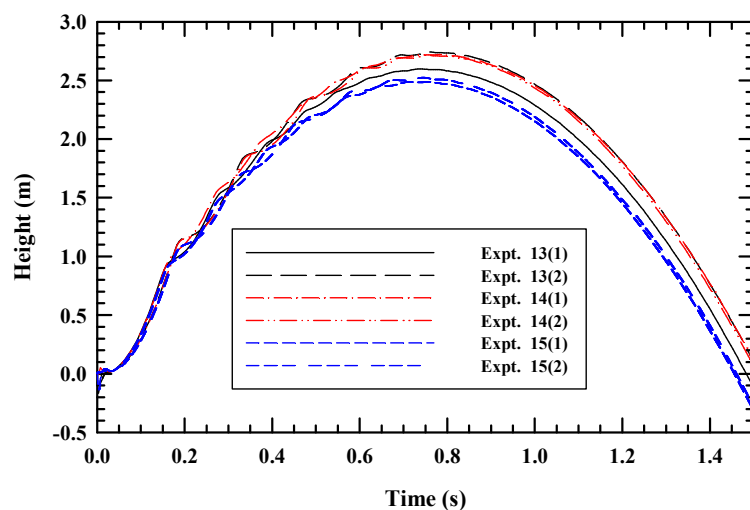


Figure 17. Potentiometer results for flat plate, 20-cm standoff, 14% moisture.

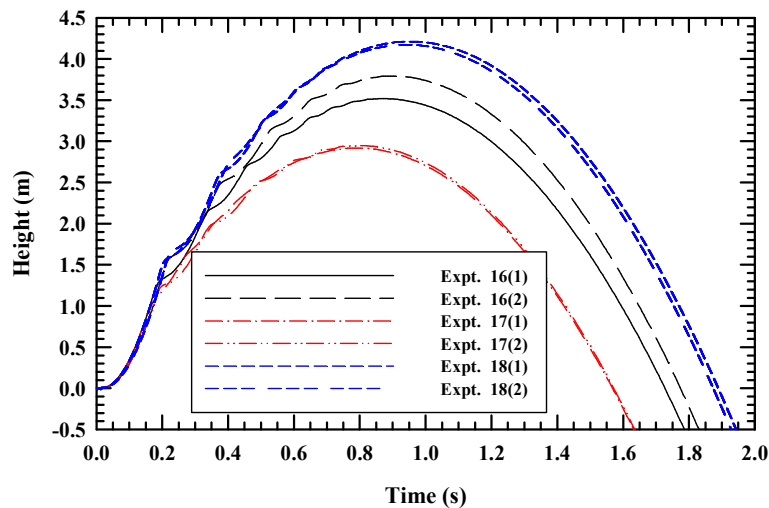


Figure 18. Potentiometer results for flat plate, 20-cm standoff, 21% moisture.

ascent occurred on Exp. 1 (Fig. 13). Typically, where there was plate tilt, it was “amplified” during descent, such in Exps. 6, 10, 13, and 16 (Figs. 14, 16, 17, and 18, respectively). Tilt was not an issue, however. Since the cables were fastened along the plate centerline (see Fig. 11), an average of the two potentiometers gives the mean height of the plate.

Table 5 provides—for each experiment—the measured moisture content, the maximum height that was recorded with each of the two cable-pull potentiometers, the maximum mean height, and the plate velocity calculated from the average height for each experiment. The last column in Table 4 gives the momentum transferred from the detonating charge to the steel plate, where the momentum transferred is defined as the product of maximum plate velocity and plate mass (using 300 kg for the flat plate, and the plate masses from Table 3 for the V-shaped plates).

**Table 5. Experimental Results**

Test No.	Exp.	Moisture Content (mass-%)	Max $H_1$ (m)	Max $H_2$ (m)	Avg. Max $H$ (m)	Plate Velocity (m/s)	Transferred Momentum (kg-m/s)
1	Flat 20	7	2.062	2.306	2.184	6.54	1963
2	Flat 20	7	2.314	2.337	2.326	6.75	2025
3	Flat 20	7	2.156	—	2.156	6.50	1950
4	Flat 30	7	1.729	1.660	1.695	5.76	1729
5	Flat 30	7	1.488	1.512	1.500	5.42	1627
6	Flat 30	7	1.408	1.326	1.367	5.18	1553
7	V-90° 25	7	0.344	0.395	0.370	2.69	830
8	V-90° 25	7	0.375	0.399	0.387	2.75	849
9	V-90° 25	7	0.297	0.320	0.309	2.46	758
10	V-120° 25	7	0.851	0.910	0.880	4.15	1285
11	V-120° 25	7	0.687	0.673	0.680	3.65	1130
12	V-120° 25	7	0.653	0.707	0.680	3.65	1130
13	Flat 20	14	2.597	2.741	2.669	7.23	2170
14	Flat 20	14	2.721	2.716	2.718	7.30	2190
15	Flat 20	14	2.487	2.523	2.505	7.01	2102
16	Flat 20	22	3.520	3.792	3.656	8.47	2540
17	Flat 20	21	2.918	2.949	2.933	7.58	2275
18	Flat 20	22	4.212	4.173	4.193	9.06	2719

Error for  $H_1$  and  $H_2$ :  $\pm 0.0113$  m (linearity of potentiometers)

### 3.2 Error Analysis of Cable-Pull Potentiometer Data

The potential error or uncertainty in the jump velocity was estimated from the possible error in the potentiometers. The jump velocity is determined from Eqn. (1). Letting the symbol  $\delta$  represent the potential error, then:

$$\delta V_j = \frac{1}{2} \sqrt{2g} \frac{\delta H}{\sqrt{H}} \quad (2)$$

where  $\delta H$  is  $\pm 0.0113$  m (the linearity of the potentiometers). Thus,  $\delta V_j$  depends upon the measured height in addition to the the possible error in the potentiometer. The potential error increases as the measured height decreases. Equation (2) is plotted as a function of the measured height in Fig. 19. The solid line shows the error in the jump velocity, while the dashed line is the percent relative error (i.e.,  $\delta V_j/V_j \times 100$ ). The lowest  $H$  measured (Table 5) was approximately 0.3 m, and for that height, the potential uncertainty in the jump velocity is  $2.42 \pm 0.046$  m/s (less than a 2% error). The error in all other experiments is less. Examining the experimental results in Table 5, it is observed that the potential error in the cable-pull potentiometer is less than the test-to-test variation.

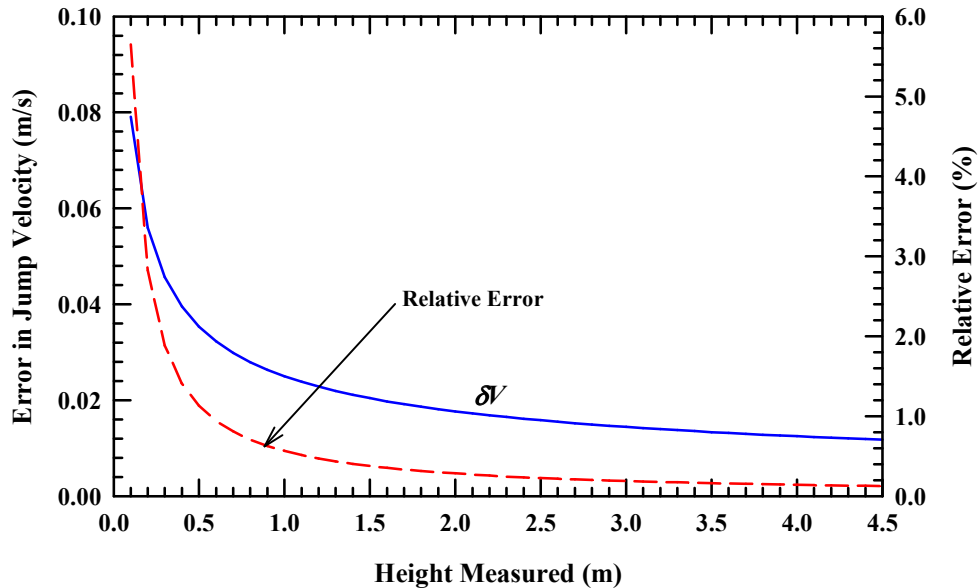


Figure 19. Potential error or uncertainty in jump velocity for measured potentiometer data.

### 3.3 Video Camera

High-speed video images were recorded for most of the flat plate experiments. Videos were normally recorded with a frame rate of 500 frames per second and an exposure time of 1/500 s. The V-shaped plate experiments produced no useable images because of the dust generation and the low maximum height of the plates.

The images from the video camera can be calibrated, and the maximum height of the steel plate can be measured. When compared to the data from the cable-pull potentiometers, good agreement is observed within 2 to 4 cm, with most of the uncertainty in the precision of

measurements from the video images because of parallax errors and pixel resolution (2 pixel difference in measuring the distance can be as much as 1.0 cm).

Figures 20 and 21 show some images from Exp. 14. Shortly after detonation, the images become very dark due to the sand dust (Fig. 20). Pictures become clearer during the fall of the plate (Fig. 21) as the dust settles. It can be seen that the plate is rotating (tilting) during fall;

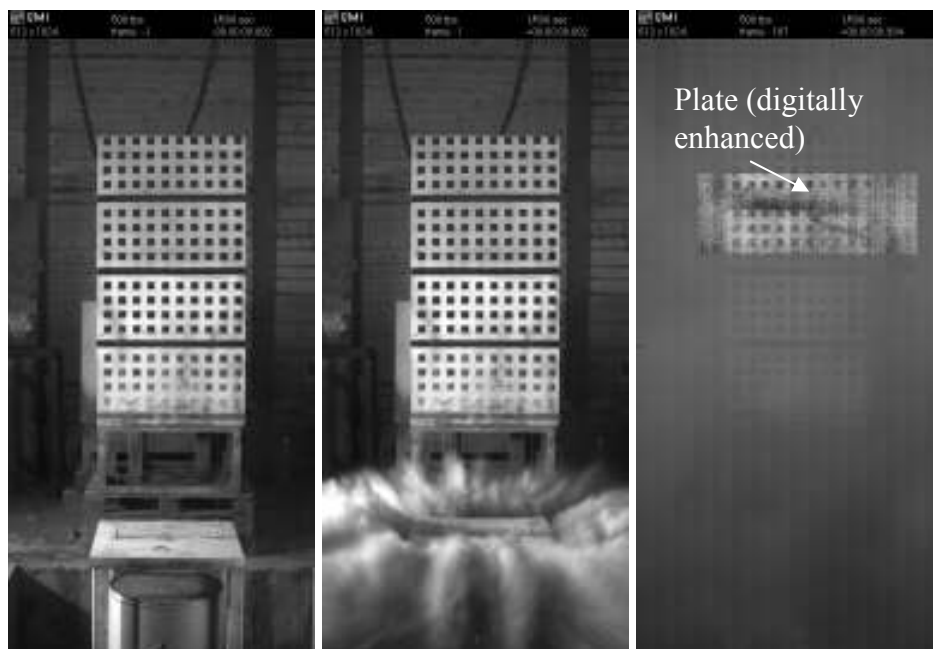


**Figure 20. Upward motion of the steel plate for Exp. 14.**

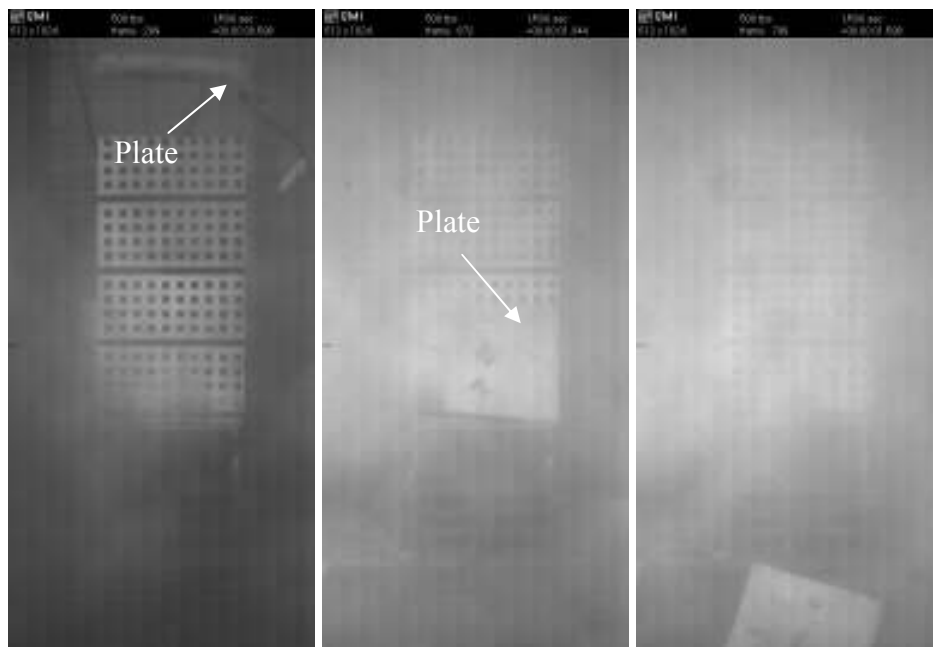


**Figure 21. Downward motion of the steel plate for Exp. 14.**

but this rotation is not recorded by the cable-pull potentiometers as the plate tilts around the centerline of the affixed cables. In Fig. 21, the plate tilts towards the reader, so that the potentiometers nominally read the same values. In other experiments, however, it is evident that the plate tilts perpendicular to the camera view, and therefore, potentiometer readings differ, as for Exp. 16 (Fig. 18).

### 3.4 Cable-Free Accelerometer

A cable-free accelerometer was placed at the center of the plate, as shown in Fig. 11. As already mentioned, the initial shock delivered to the plate resulted in sensor/recorder malfunction. Because of repair time, the recorder was not available for every experiment, but it functioned successfully for Exp. 18. The acceleration-time results are shown in Fig. 22.<sup>3</sup> The ordinate and abscissa are expanded in Fig. 23 to permit better resolution of the acceleration data. Typically, acceleration data are analyzed in terms of the gravitational constant,  $g$  ( $9.8 \text{ m/s}^2$ ). Since  $9.8 \text{ m/s}^2 \approx 10 \text{ m/s}^2$ , dividing the ordinate results in Figs. 22 or 23 by 10 provides a very good approximation of the loading in  $g$ 's.

The data show accelerometer readings up to 3000  $g$ 's at very early times. After the first initial spike, peak accelerations of  $\sim 50 \text{ g}$ 's are recorded. The plate will have large particle velocities as the plate rings elastically from loading by the sand and blast. These large particle velocities are transferred to the accelerometer housing. However, these accelerations are extremely short in duration. Additionally, any connecting elements in a more complicated structure would tend to "filter" this very high-frequency response.

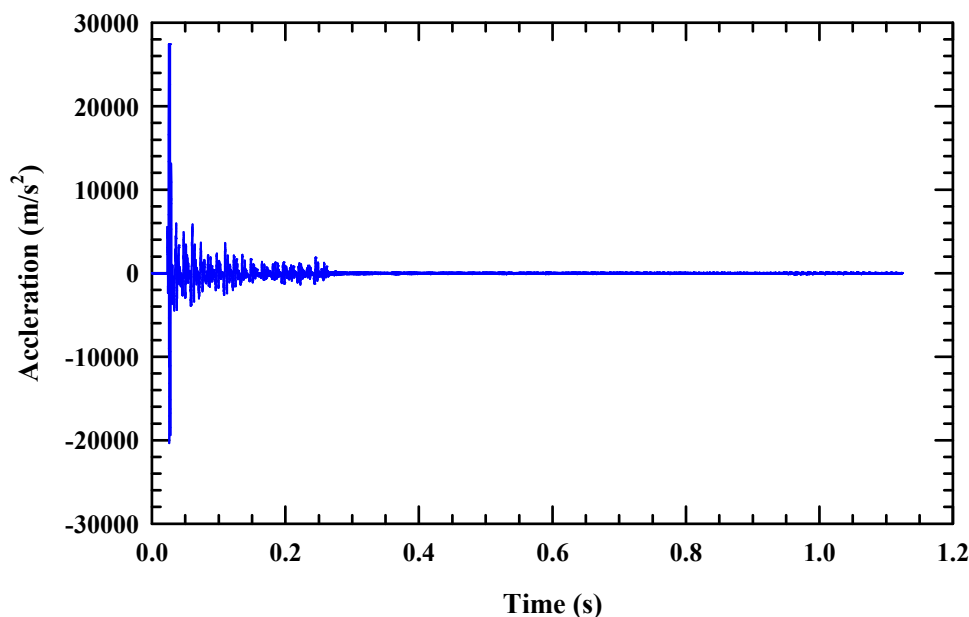
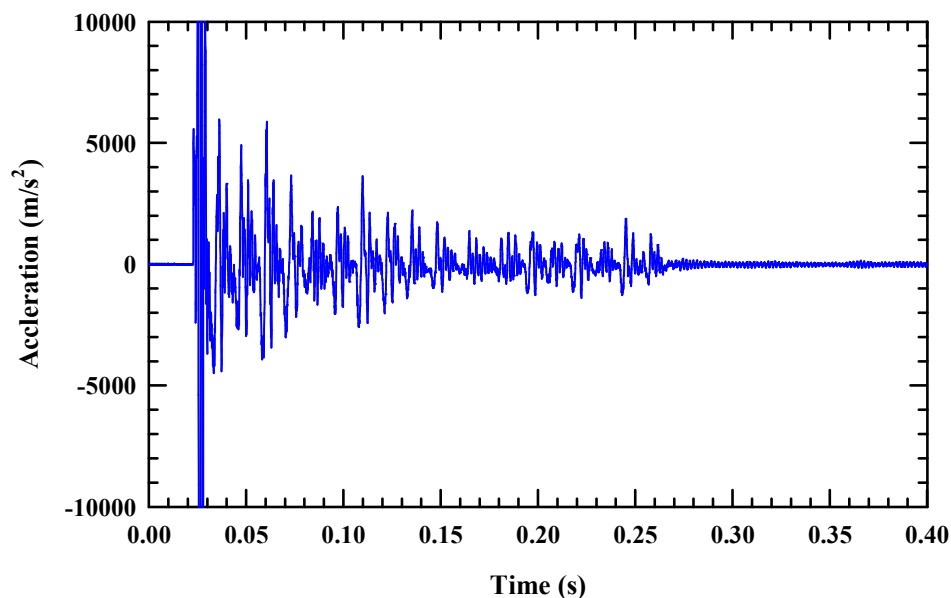


Figure 22. Acceleration-time for Exp. 18.

<sup>3</sup> The readings from the accelerometer recording system were not filtered as double time integration eliminates any peaks/spikes effectively. However, as the acceleration recording system is cable free, time "0" had to be adjusted manually to coincide with initiation of the explosive.



**Figure 23. Expanded scales for the ordinate and abscissa axes of Fig. 22.**

Single time integration of the acceleration-time results gives the velocity-time response of the plate, Fig. 24. A peak velocity of 16 m/s is shown; and even if a filter is applied to the accelerometer data, some peak readings of  $\sim 12$  m/s are seen. Extrapolation of the smoother portion of the velocity-time response back to time zero gives a value of approximately 9 m/s for the jump velocity. This is in very good agreement with the 9.06 m/s calculated from the potentiometer data. At approximately 0.97 s, the plate velocity goes through zero (signifying that the plate has reached its maximum height), and the plate begins to fall back towards the test pit. (It is noted that the slope of the velocity-time curve is  $-g$ , as it should be.)

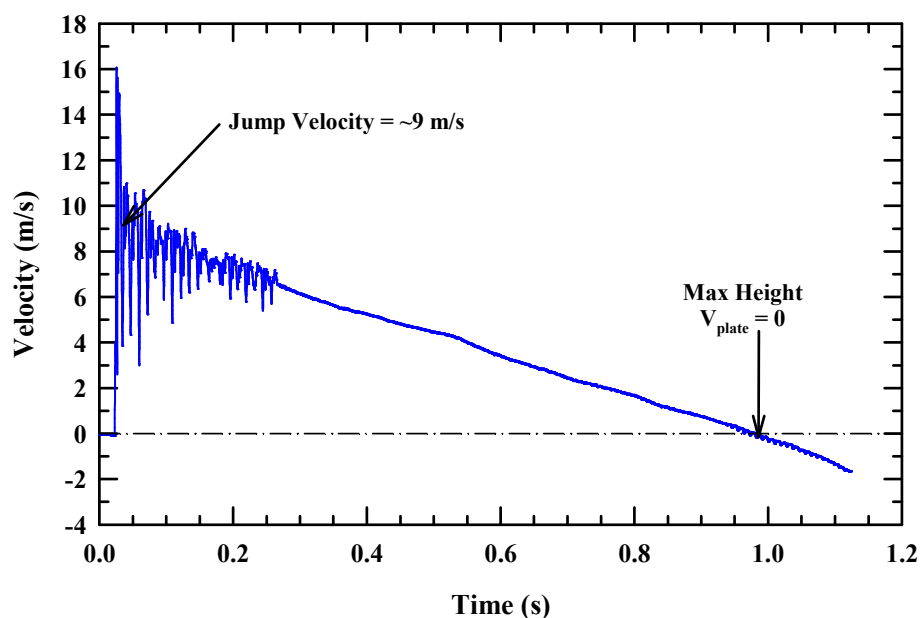


**Figure 24. Velocity-time for Exp. 18, from time integration of the data in Fig. 22.**



Time integration of the velocity-time data gives the displacement-time history of the plate, which is shown in Fig. 25. Double time integration of the acceleration data yields very smooth displacement-time data. Maximum height from this is 4.18 m, denoted by the callout in the figure. This is in excellent agreement with the 4.193 m given by the average of the potentiometer data for Exp. 18, which are plotted as the dashed lines in Fig. 25. As already stated, the cable-pull potentiometer cannot wind the cable sufficiently fast to follow plate motion at early times. This very good agreement for the maximum displacement from the cable-free accelerometer and the cable-pull potentiometers demonstrates that the cable-pull potentiometers are reliable.

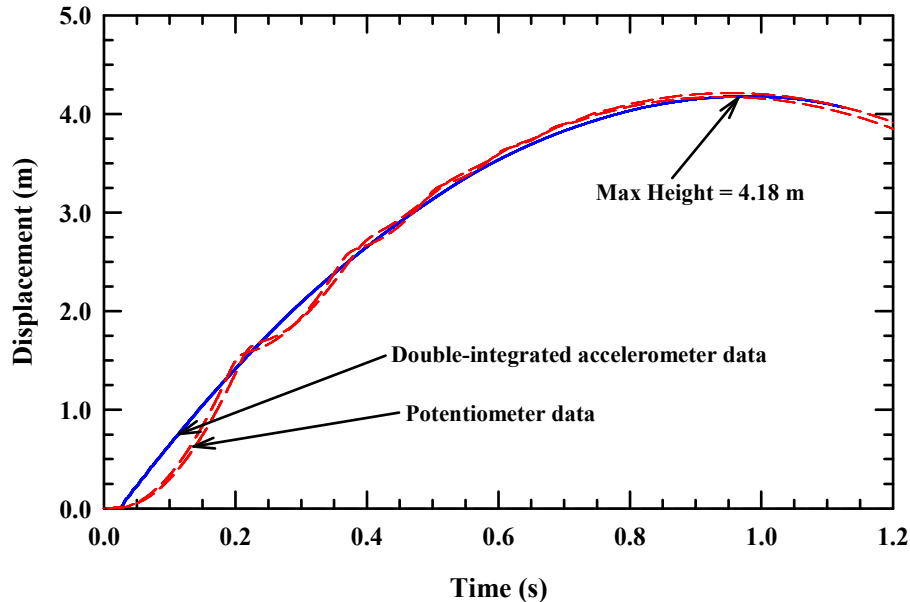


Figure 25. Displacement-time for Exp. 18, from time integration of the data in Fig. 24.

### 3.5 Analysis of Experimental Results

The height-versus-time responses of the plates were shown in Section 3.1. The maximum heights were used to determine the jump velocities, Eqn. (1), and are listed in Table 5. These results are shown graphically in Fig. 26 for the flat-plate and V-shaped plate experiments conducted with the nominal 7% moisture sand. The averages of the three similar experiments, along with the standard errors, are shown in Fig. 27. As already indicated, reproducibility was, in general, quite good.

The momentum transferred to the plates is the plate mass (300 kg) times the jump velocity. As expected, the momentum transferred to a flat plate decreases with increasing standoff distance (200 mm to 300 mm). It is also observed that as the standoff increases, there is somewhat more variability in the transfer of momentum from the soil to the plate; perhaps because with the increased standoff distance, there is more time for development of the Richtmyer-Meshkov instability described by Taylor, et al. [18].

It is seen that the V-shaped plates, with a standoff of 250 mm, have significantly less momentum transferred from the sand than for the flat plates at either the 200-mm or 300-mm standoffs. Further, the steeper (or sharper) the V, the less momentum transferred to the plate. Presumably, this is because the sand and explosive products no longer stagnate against the plate, but can flow along the plate, significantly reducing momentum transfer. This is true even though

the lower portion of the V is closer to the soil surface directly above the buried HE charge; and we have observed that the effects of the mine blast are predominantly focused directly above the charge.

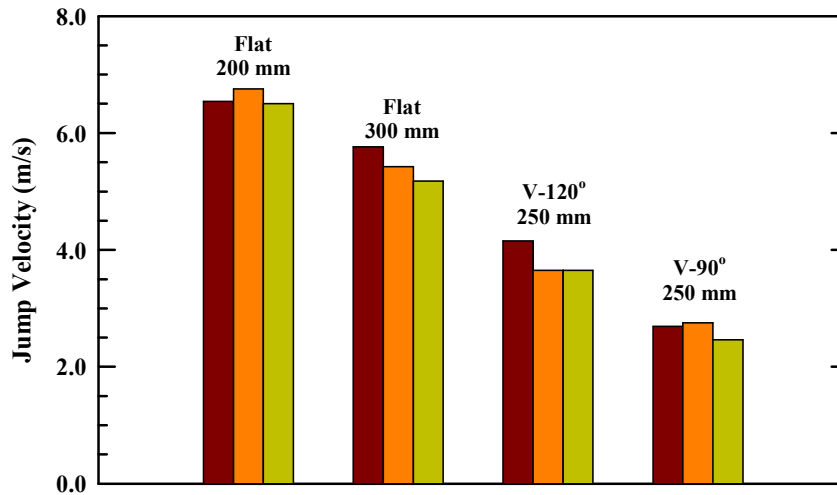


**Figure 26. Comparison of calculated jump velocities for flat-plate and V-shaped plate experiments.**

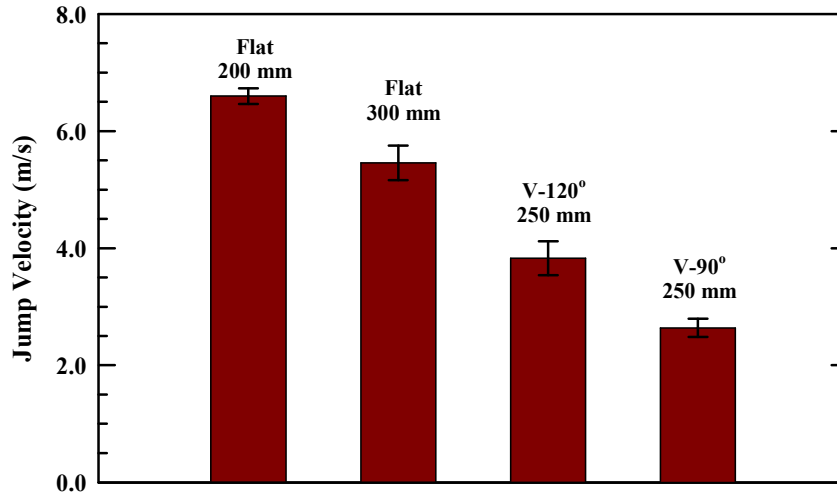


**Figure 27. Jump velocities with standard errors for flat-plate and V-shaped plate experiments.**

Similar plots for the flat-plate experiments, all positioned at 200 mm above the soil surface, as a function of sand moisture content are shown in Figs. 28 and 29. The largest variability in the results are for the highest moisture content; whereas the experiments using sand with 7% and 14% moisture content demonstrate very good reproducibility.

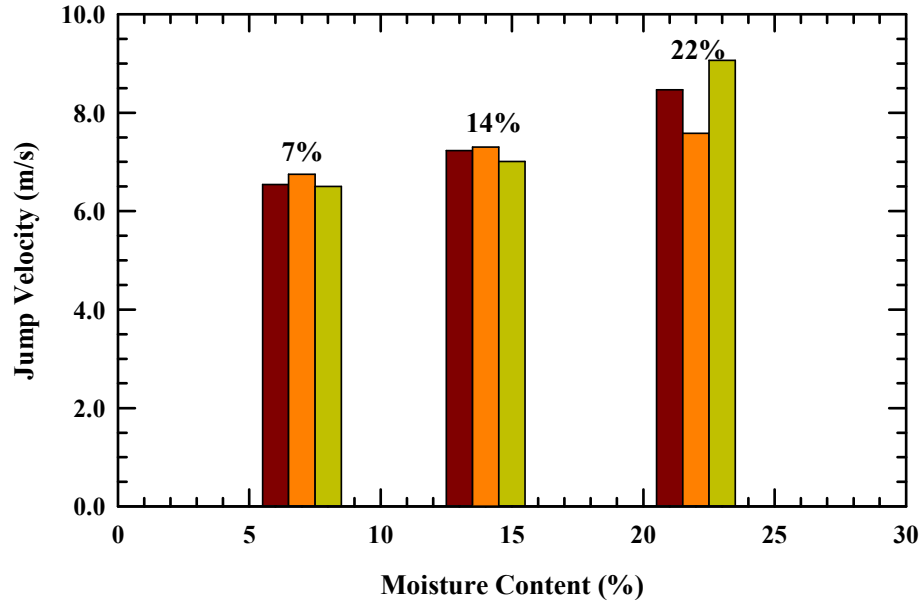


**Figure 28. Comparison of calculated jump velocities for flat-plate experiments vs. sand moisture content.**

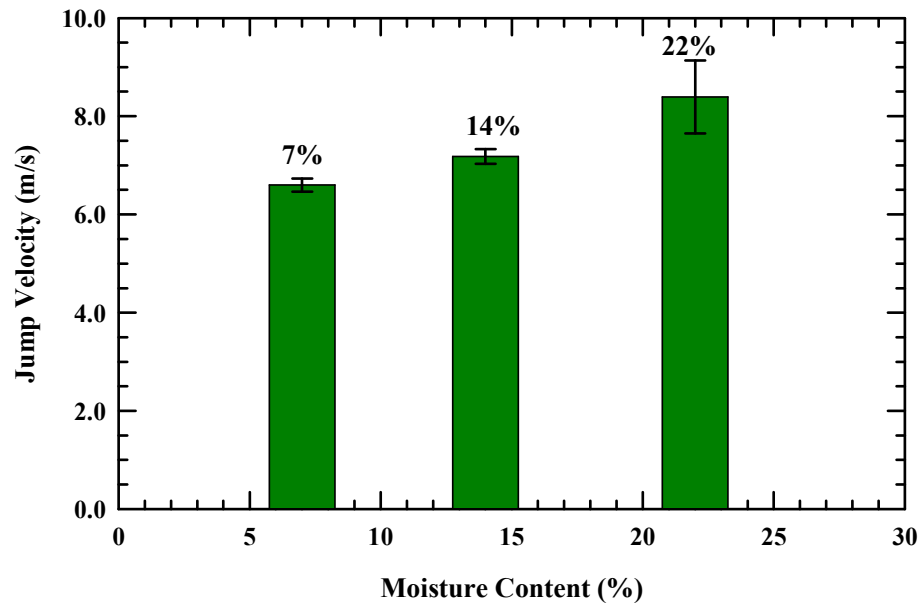


**Figure 29. Jump velocities with standard errors for flat-plate experiments vs. sand moisture content.**

The momentum transferred to the flat plate as a function of moisture content is plotted in Fig. 30. The data points are the same data as plotted in Fig. 29, but now the ordinate is the jump velocity times the plate mass (i.e., plate momentum). Heider and Klomfass [22] showed computationally that the initial soil density had a considerable effect on the radial specific momentum distribution of the loaded plate. From Table 2, it is seen that soil density depends upon the moisture content, with the density increasing with moisture content over the range investigated. Sand density as a function of moisture content for these experiments is shown in

Fig. 31; the density is not quite linear with moisture content, but linearity would be a reasonable approximation.

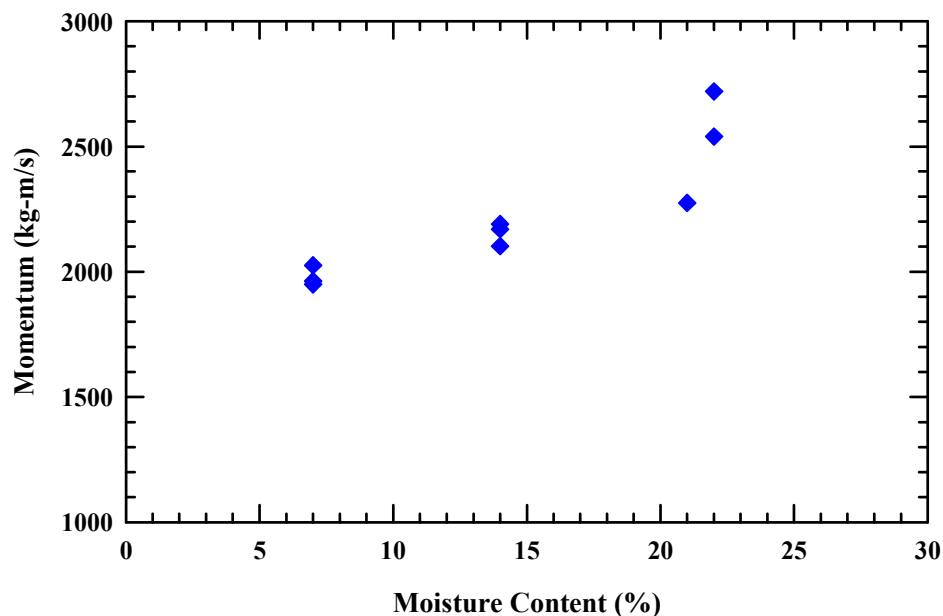


Figure 30. Plate momentum as a function of moisture content (20.0-cm standoff).

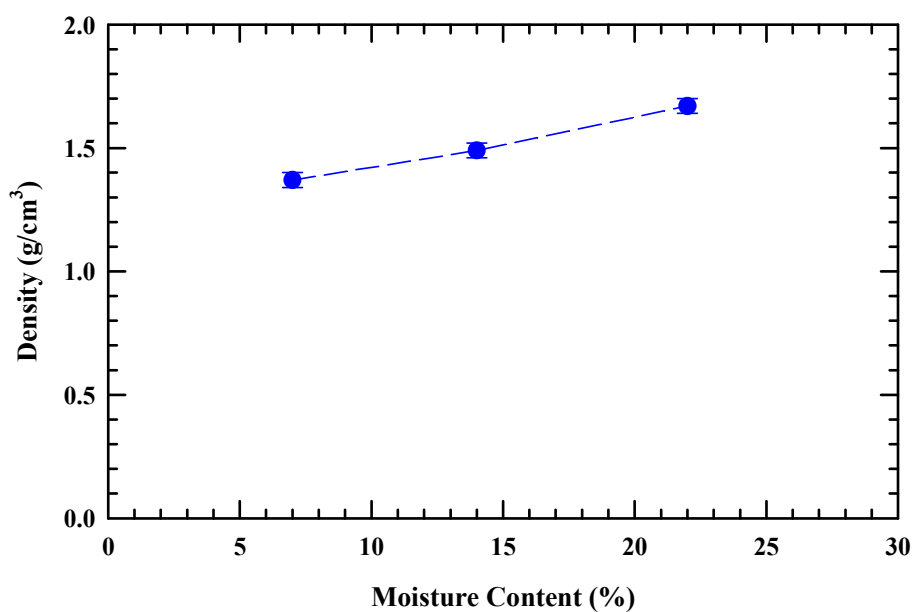
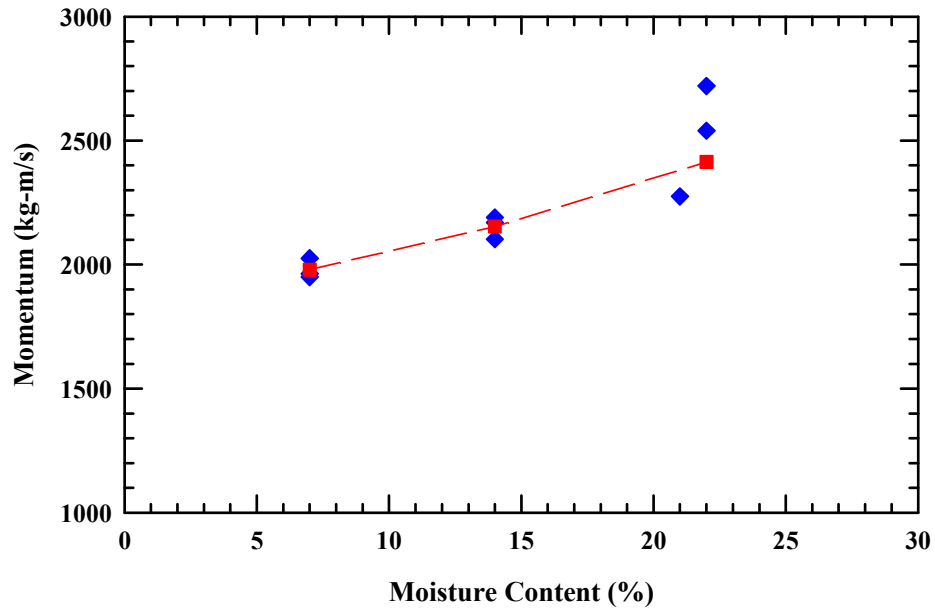


Figure 31. Measured sand density as a function of moisture content.

If it is assumed that the transferred momentum,  $M$ , is a function of soil density,  $\rho$ , then plate momentum can be computed for the 14% and 22% moisture content by taking the plate momentum at 7% moisture content as a reference point:

$$M_k = \left( \frac{\rho_k}{\rho_7} \right) M_7 \quad (3)$$

where the subscript  $k$  refers to the density, and the subscript “7” refers to the density and plate momentum at 7% moisture content. The results of using Eqn. (3) are plotted in Fig. 32. These calculated values for the plate momentum show good agreement with the values obtained from the experiments, suggesting that the a major contribution to the observed increase in mometnum transferred with increasing soil water content is due to density effects.



**Figure 32. Transferred momentum vs. moisture content (20.0-cm standoff); the overlaid squares show the relation between momentum and sand density.**

UNCLASSIFIED

UNCLASSIFIED

## 4.0 Numerical Simulations

### 4.1 Introduction

Numerical simulations were conducted to investigate how accurately they might replicate the experiments. The numerical simulations were performed using the nonlinear, large deformation, multi-material Eulerian wavecode CTH [34]. CTH uses a van Leer algorithm [35-36] for second-order accurate advection that has been generalized to account for a nonuniform and finite grid, and multiple materials. CTH has an advanced material interface algorithm for the treatment of mixed cells. Also, CTH has been modified to allow the flow stress to be a function of strain, strain rate, and temperature [37-38].

### 4.2 Equation of State for Sand

#### 4.2.1 Review of Sand EOS in CTH

CTH contains various soil equations of state (EOS) developed by Kerley [29,33], where he treated the soil as a three-component mixture with solid grains, water, and voids. The following definitions and relations are useful for computing some of the parameters required for the EOS:

$\rho_o$	initial soil density (including water and air-filled voids);
$\rho_{Moist\ Soil}$	density of compacted soil (which is a function of water content);
$\rho_s$	solid (grain) density = 2.648 g/cm <sup>3</sup> ( $\equiv \rho_{quartz}$ );
$\rho_w$	density of water = 1.0 g/cm <sup>3</sup> ;
$\rho_d$	dry density (density if water is replaced by air);
$w$	moisture content = weight of water divided by weight of dry soil;
$\phi$	void fraction (volume fraction of water and air).

Kerley used the PANDA code to construct the EOS sesame tables for soil from the mixture of solid grains and varying amounts of water (4%-24%). The EOS numbers, percentage moisture, initial density, and compacted density are shown in Table 6. The EOS tables describe the material after all pores have been compacted. Kerley used alpha-quartz, with a density of 2.648 g/cm<sup>3</sup>, as the fully compacted soil ( $\rho_s$ ) without water. Assuming equal temperatures and pressures, and that the volumes of the two components (water and quartz) are additive, then:

$$\begin{aligned} V_{Moist\ Soil} &= V_w + V_{quartz} \\ \frac{M_{Moist\ Soil}}{\rho_{Moist\ Soil}} &= \frac{M_w}{\rho_w} + \frac{M_{quartz}}{\rho_{quartz}} \end{aligned} \quad (4)$$

where  $V$  and  $M$  represent the volume and mass, respectively of the components. By definition,  $w = M_w/M_{quartz}$ , and  $M_{Moist\ Soil} = (1+w)M_{quartz}$ . Using these definitions and rearranging, then the relationship between the density of the moist soil, water content, and solid (quartz) material is given by:

$$\rho_{Moist\ Soil} = \frac{1+w}{\rho_w + w\rho_{quartz}} \rho_w \rho_{quartz} \quad (5)$$

The compacted densities as a function of water content for sand are shown in Table 6.

**Table 6. Moisture content and initial densities for the different soil models developed by Kerley [33] and implemented into CTH.**

EOS #	Moisture $w$ (% weight)	Initial Density $\rho_o$ (g/cm <sup>3</sup> )	Compacted Density $\rho_{Moist Soil}$ (g/cm <sup>3</sup> )
7860	4	1.686	2.486
7861	6	1.72	2.418
7862	8	1.75	2.355
7863	10	1.78	2.298
7864	12	1.82	2.245
7865	14	1.85	2.197
7866	17	1.90	2.130
7867	20	1.95	2.071
7868	24	2.01	2.001
EMI-7	7	1.37	EOS #7861
EMI-14	14	1.49	EOS #7865
EMI-22	22	1.67	EOS #7867

A distinction is made between fully compacted soil (alpha quartz and water), and the sand that is used in the test bed. Here, the sand has considerable porosity. The dry sand has a density of  $\rho_d$ ; the porosity or void fraction  $\phi$  is given by:

$$\phi = 1 - \frac{\rho_d}{\rho_{quartz}} \quad (6)$$

The initial soil density is given by:

$$\rho_o = \rho_d(1 + w) \quad (7)$$

For the Kerley-CTH models,  $\rho_d = \sim 1.625$  g/cm<sup>3</sup>. Using this value for  $\rho_d$ , and the corresponding values for  $w$ , the initial densities shown in Table 6 were calculated.

Porosity is treated using the  $p$ - $\alpha$  model [30]. The EOS of the porous material is related to that of the void-free material by [33]:

$$P(\rho, T, \alpha) = \frac{P_s(\rho, T, \alpha)}{\alpha} \quad E(\rho, T, \alpha) = E_s(\alpha\rho, T) \quad (8)$$

where the functions  $P_s$  and  $E_s$  define the EOS for the void-free material, which is one of the tabular EOS listed in Table 6. The parameter  $\alpha$  represents the irreversible compaction of pores, where the initial distention is given by:

$$\alpha_o = \frac{\rho_s}{\rho_o} \quad (9)$$

where  $\rho_s$  is the density of the void-free material and  $\rho_o$  is the initial density. It is assumed that  $\alpha$  is only a function of pressure:

$$\alpha = 1 + (\alpha_o - 1)(1 - P/P_C)^2 \quad (10)$$



where  $P_C$  is the pore compaction pressure, i.e., the pressure at which the pores have been completely collapsed, at which point,  $\alpha = 1$ . Kerley notes [29] that while other forms of pore collapse besides Eqn. (10) can be used, simulations show that the impulse delivered to the plate is relatively insensitive to the exact form. This was also demonstrated by Heider and Klomfass [22]. Thus, only two parameters are required for the  $p$ - $\alpha$  model, the initial density and  $P_C$ . Kerley found that a value of  $P_C = 0.25$  GPa provided a reasonable fit to the low-pressure behavior of sand.

#### 4.2.2 Modifications to the EOS for the Current Experiments

The initial densities of the sand as a function of moisture content for the experiments reported here are given in Table 2, and also are listed in the last 3 rows of Table 6. These densities are different than the ones assumed for the various EOS formulations as a function of moisture content in CTH (Table 6). However, the only parameter that required changing was the initial density used by the  $p$ - $\alpha$  model for calculating  $\alpha_o$ . These densities are smaller than the ones used in the CTH library implying that additional porosity is initially present; i.e., the dry sand density is approximately  $1.30 \text{ g/cm}^3$ , instead of the  $1.625 \text{ g/cm}^3$  assumed by Kerley.

The pressure versus density response obtained when hydrostatic compression and extension cycles are applied to the 14% water EOS is shown in Fig. 33. One curve (blue) uses the “as given” density for EOS #7865 (see Table 6) with an initial sand density of  $1.85 \text{ g/cm}^3$ . The initial density of 14% water for the EMI experiments was  $1.49 \text{ g/cm}^3$ , and this response is shown as the red curve.<sup>4</sup> With the EMI density, compaction starts out at a smaller density because of the higher porosity content, but full compaction occurs at a similar pressure and density as the less porous soil.

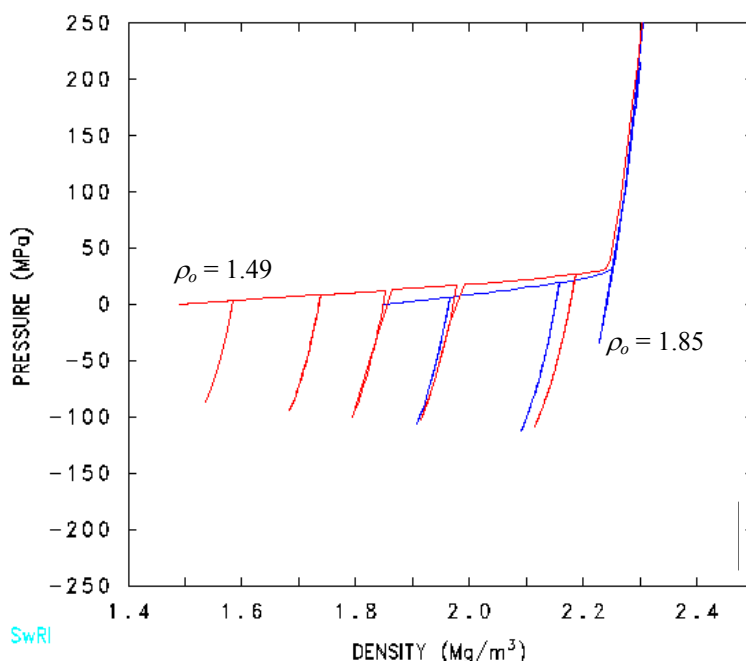


**Figure 33. Pressure vs. density response for 14% moisture content with different initial soil densities (porosities).**

<sup>4</sup> The general  $p$ - $\alpha$  model allows for the definition of an elastic response in which the compaction is reversible. Any elastic response is ignored for the soil model, and “crushing” begins immediately with applied pressure.

The moisture content for the EOS's developed by Kerley increases by 2% for the lower levels of moisture content and 3% for higher levels of moisture content. The pressure versus density responses of 6% and 8% moisture content, which bracket the 7% moisture content of many of the experiments reported here, are shown in Fig. 34. The 8% EOS was started at the same initial density as the 6% curve ( $1.72 \text{ g/cm}^3$ ). The compaction curves are approximately the same for the two moisture contents, but “lock up” occurs at a slightly lower pressure and density for the soil with the higher moisture content (8%) since water is more compressible than solid alpha quartz. We elected to model the 7% moisture content with the 6% EOS, but it will be shown in Section 4.6.2 that either the 6% or the 8% EOS could be used (assuming the correct initial density).

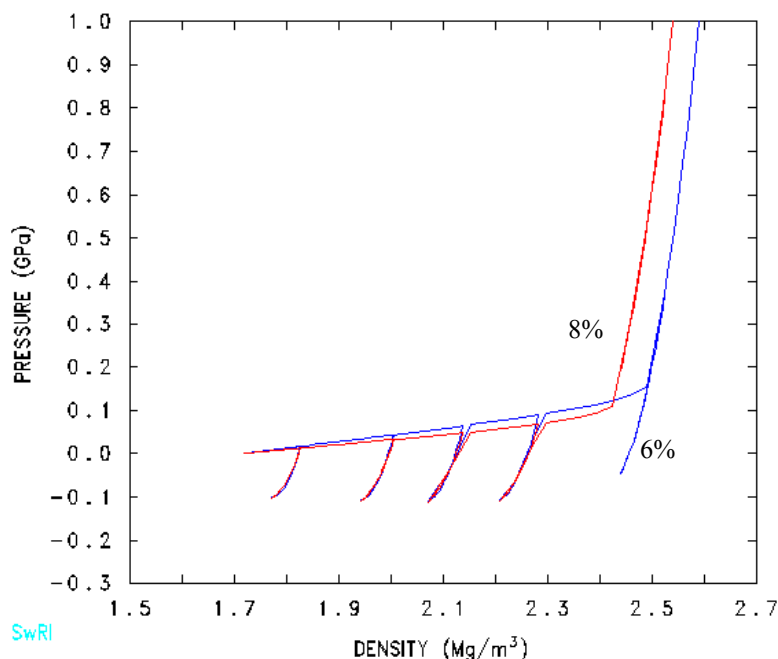


**Figure 34. Pressure vs. density response for two different moisture contents with same initial density.**

### 4.3 Strength and Fracture Model

The CTH geological model was used to account for strength of the soil:

$$Y(P) = Y_{\max} + (Y_0 - Y_{\max}) \exp(\beta P / (Y_0 - Y_{\max})) \quad (11)$$

with the parameters suggested by Kerley [33] for concrete sand:

$$Y_0 = 0.3 \text{ MPa,}$$

$$Y_{\max} = 160 \text{ MPa (7%); } = 99 \text{ MPa (14%); } = 56 \text{ MPa (22\%)}$$

$$\beta = 2.0$$

A Poisson's ratio of 0.32 was used, and the melt temperature was  $1468^\circ\text{C}$ . The fracture stress was assigned to be  $-0.3 \text{ MPa}$ .

#### 4.4 Explosive Charge Mass for Simulations

The charge mass, as measured for each experiment, was 625 g. The mass of the explosive is accurate; however, the dimensions reported in Section 2.4 should be considered as approximate. For the simulations, using a diameter of 11.3 cm, a height of 3.7 cm, and a density of 1.717 g/cm<sup>3</sup> for Comp B, the computational charge mass is 637 g. This increase in the charge mass approximately accounts for the extra energy in the initiator. In Section 4.6.3, the effect of slightly different charge masses is quantified.

#### 4.5 Grid Convergence Study

A series of simulations was conducted to investigate appropriate grid resolution. The simulations were first conducted using the 2-D cylindrically symmetric option in CTH. The steel plate in the real experiments is square. A cylindrical disk with a diameter equal to the length of the side of the square plate, but with a thickness of 7.64 cm (as opposed to the 6-cm-thick square plate), was used to model the 300-kg plate. An output of CTH is the momentum components of each material at each time step. Therefore, it is easy to plot plate momentum versus time. The results for 6 different grid resolutions are shown in Fig. 35 for the 20-cm standoff, and Fig. 36 for the 30-cm standoff. The datum point plotted at 4.75 ms represents the average momentum from the experiments, along with one standard deviation about the average. The point is plotted at 4.75 ms for convenience, and is not intended to indicate that the experimentally measured plate momentum was obtained at 4.75 ms.

Grid sizes ranged from 3.0-cm wide cells to 0.25-cm wide cells (square zoning was used throughout the computational domain). Absolute size of a computation cell is not the criterion for grid resolution; rather, it is the number of computational cells required to resolve important features of the problem. Referring to Fig. 1, it is seen that the various zone sizes permit the resolutions as shown in Table 7.

**Table 7. Number of Zones Resolving Elements of Mine Blast Loading Problem**

	Zone Size (cm)					
	3.0	2.5	2.0	1.0	0.50	0.25
<b>HE radius</b>	1.88	2.26	2.82	5.65	11.3	22.6
<b>HE thickness</b>	1.23	1.48	1.85	3.7	7.4	14.8
<b>Top of HE to soil surface</b>	1.67	2.0	2.5	5.0	10.0	20.0
<b>Soil surface to steel plate</b>	6.67	8.0	10.0	20.0	40.0	80.0
<b>Plate thickness: 3-D</b>	2.0	2.4	3.0	6.0	12.0	24.0
<b>Plate thickness: 2-D</b>	2.55	3.06	3.82	7.64	15.3	30.6

Although there is variability in the results as a function of mesh resolution, the general trend in Figs. 35 and 36 is for the plate momentum to level off between ~1.5 – 2.0 ms, followed by a slight rise in momentum at ~2.5 ms (for the 20-cm standoff) or ~3.0 ms (for the 30-cm standoff). This slight increase in momentum is most likely a result of the reflection of the initial blast wave from the bottom of the test article. After this slight increase, the plate momentum again levels off by ~4.5–5.0 ms. It is observed that a few of the simulations may still be “drifting” slightly higher in momentum. We believe this to be the result of the large numerical eddies that are a function of grid resolution, which will be discussed below. For consistency, we have elected to take the simulated plate momentum at 4.75 ms for comparisons with experimental results.

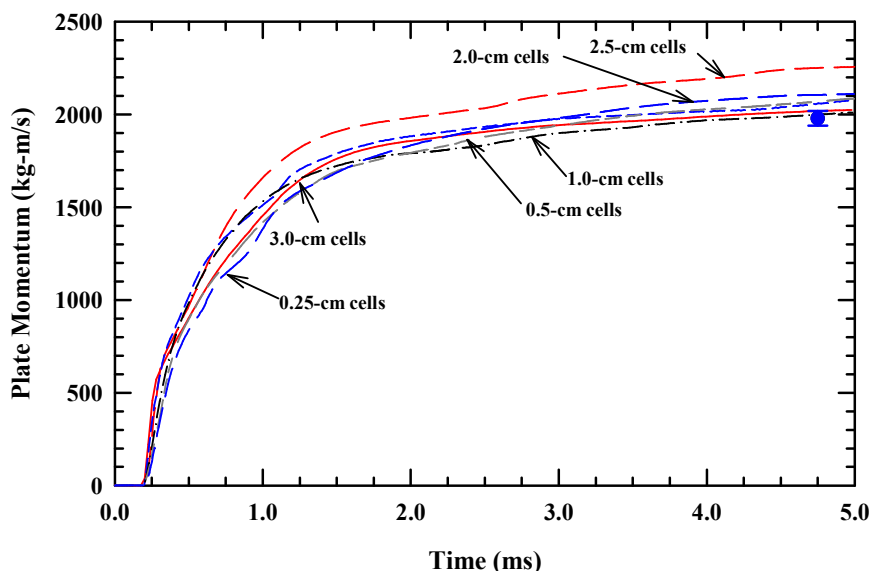


Figure 35. Plate momentum vs. grid resolutions: 2-D simulations—20-cm standoff.

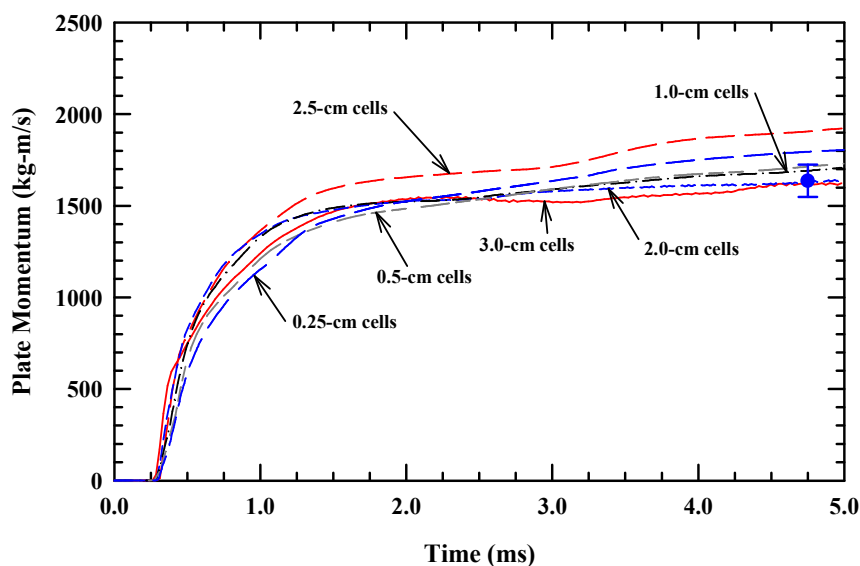


Figure 36. Plate momentum for various grid resolutions: 2-D simulations—30-cm standoff.

Numerical convergence oscillates about the converged value, which is more readily apparent in the 30-cm standoff problem; e.g., 3.0-cm cells predicts a value that is a little low, while 2.5-cm cells predict a value that is a little high. This is in contrast to penetration problems, where convergence is monotonic [40]; that is, as grid resolution is improved, the “convergence variable”—such as depth of penetration—converges to a solution from one direction. The difference between these two problems is that for penetration, improved grid resolution provides more accurate estimates of the penetration stresses; whereas, for the mine blast problem, convergence is assessed on the final momentum of the plate, and the codes are excellent at conserving momentum. Alternatively, if pressure had been used as the convergence criterion, results may well have been different. For the purposes here, it was assessed that the 1-cm grid provided sufficient resolution for accuracy in 2-D, while allowing for relatively rapid (~1 CPU hour) solutions. These 2-D results then provide a “standard” for comparing simulations conducted in three dimensions.

Although the final momentum-time converges to a nominal value, the initial rise does not converge to a common response; that is, the early momentum-time results are mesh-size dependent. This is attributed to the Richtmyer-Meshkov instability (RMI) [18], which can be considered as a special case of the Rayleigh-Taylor instability. The Rayleigh-Taylor instability is an instability that occurs at the interface of two fluids of different densities when the lighter fluid is pushing the heavier fluid. The RMI occurs at the interface between fluids of different densities impulsively accelerated. The instabilities grow with time. For the RMI, bubbles appear for the case of a light fluid penetrating a heavy fluid, and spikes (or fingers) appear for the case of a heavy fluid penetrating a light fluid. For the landmine case, both conditions occur: detonation gases push against the granulated soil, and the soil pushes against the air above it. The instabilities result in different load-time histories as grid resolution is changed. This results in a “final” plate momentum that might have a slight variability associated with mesh size. RMI will be discussed further in reference to the V-shaped plates.

Three-dimensional simulations were conducted next. The plate is now modeled as a square plate with a thickness of 6.0 cm. One plane of symmetry was used. The number of zones resolving various elements of the problem remains the same as shown in Table 7. The results as a function of zone size (cubic zones) are shown in Fig. 37. There is approximately a 5% difference in final plate momentum as a function of zone size ( $2200 \pm 100 \text{ kg-m/s}^2$ ). It was concluded that the 1-cm zone size provided a good compromise in resolution versus run times for 3-D simulations. The plate momentum is approximately 5% larger for the 3-D 1.0-cm zones compared to the 2-D solution using 1-cm zones. In addition to variation of the final plate momentum to zone-size resolution, some differences in the 2-D and 3-D results can be attributed to the differences in plate geometry (a cylindrical disk versus a plate) since the 3-D flat plate has 27% more surface area than the cylindrical plate. A 3-D simulation of the 300-kg circular plate reproduced the 2-D cylindrically symmetric result, which provides confidence that 1-cm zoning in 3-D provides a numerically resolved solution.

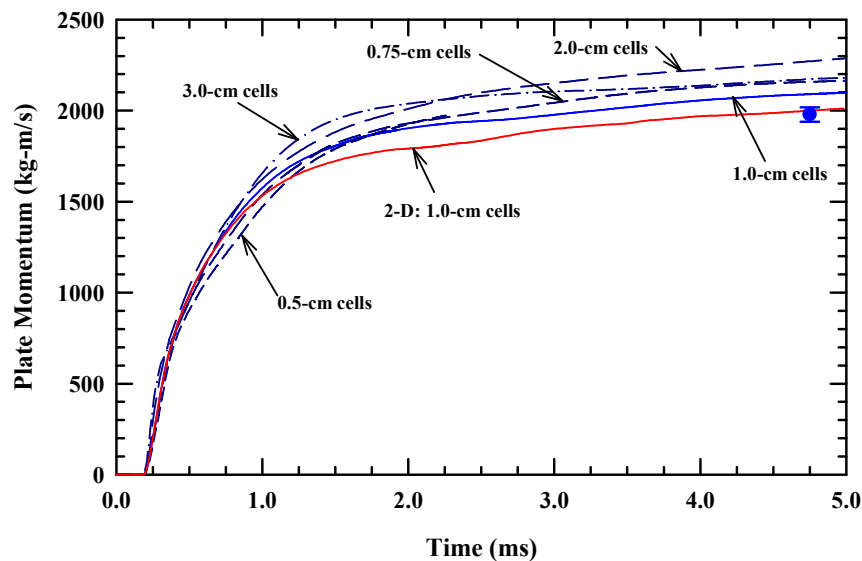


Figure 37. Plate momentum for various grid resolutions: 3-D simulations—20-cm standoff.

#### 4.6 Flat Plate Simulations

Simulations of the flat-plate experiments will be analyzed first. Cylindrically symmetric simulations are used to examine overall response, and to assess the influence of equation of state

assumptions, small changes in HE mass, and the effect of soil strength on total impulse transferred to the plate. Next, results of 3-D simulations of the actual experiments will be compared to the experimental results for the three different moisture contents and two standoff distances. Conclusions are then summarized. Section 4.7 will discuss simulations of the V-shaped plates.

#### 4.6.1 2-D Simulations

Sequences of material and pressure contour plots are shown in Figs. 38 and 39, respectively, for the 7% moisture content with the plate at 20-cm standoff. The initial soil bubble and plate

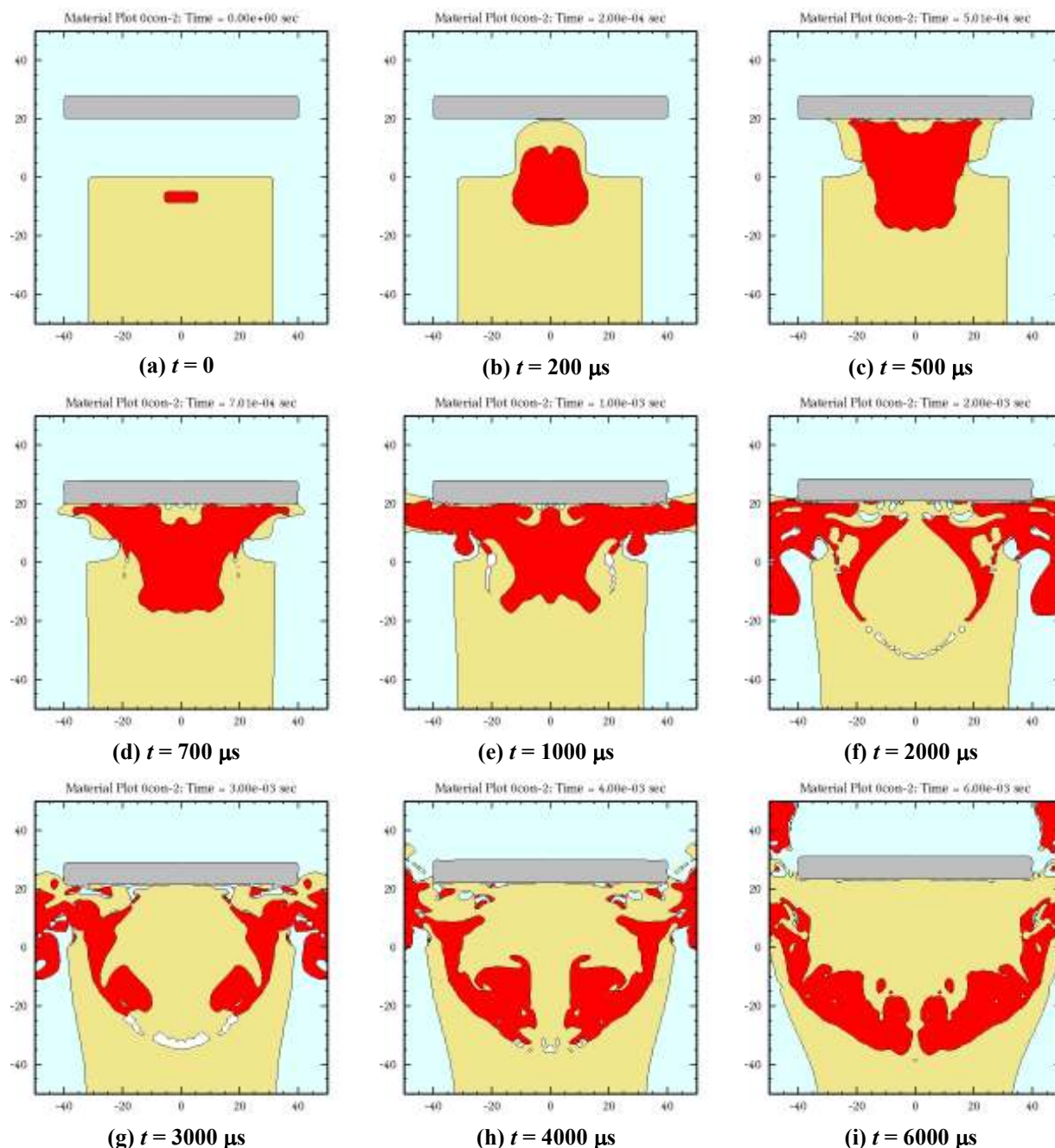
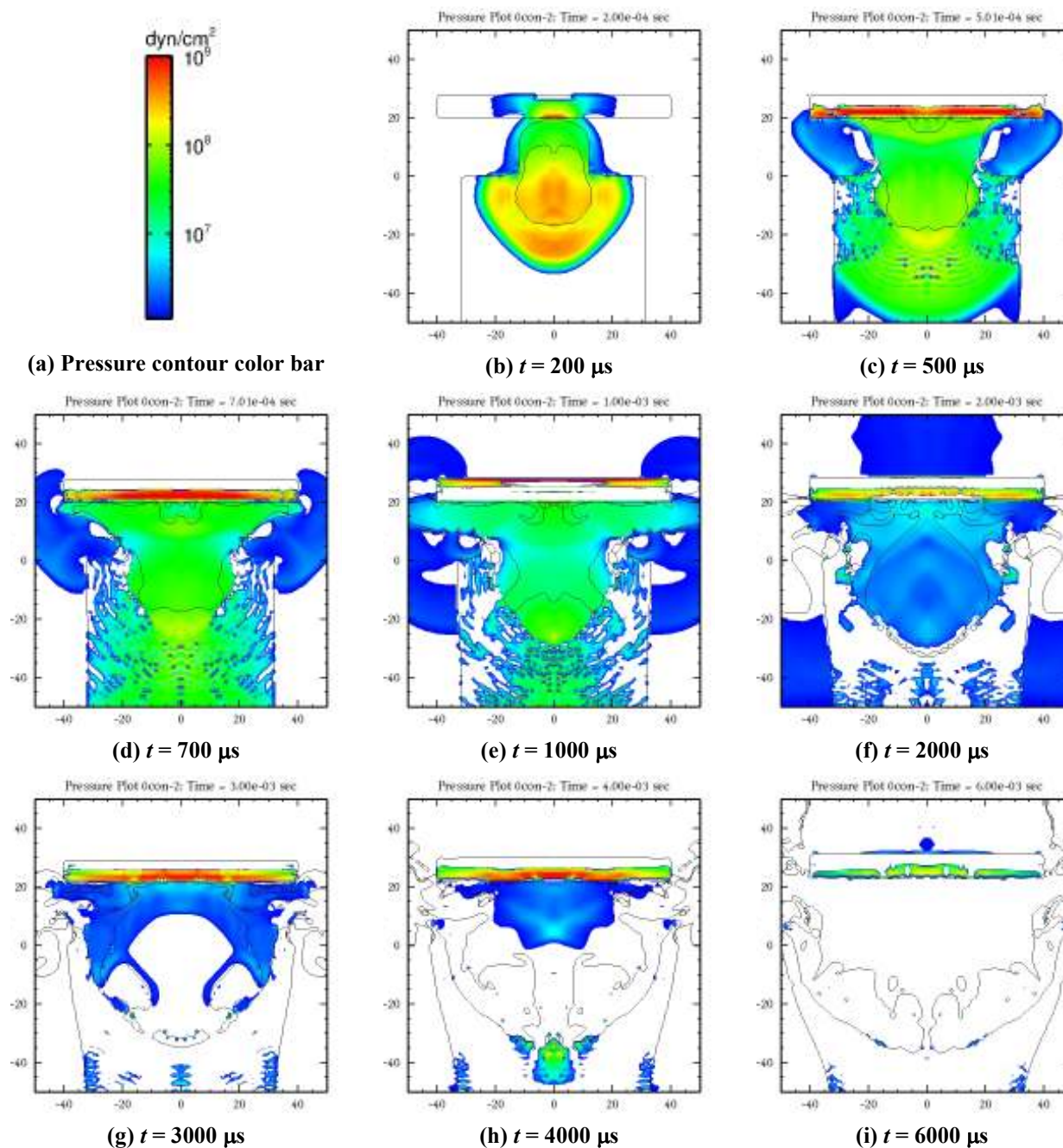


Figure 38. Material plots of mine blast loading of flat plate at 20-cm standoff.





**Figure 39. Pressure contours for mine blast loading of flat plate at 20-cm standoff.**

loading is concentrated above the charge. The debris and explosive gases then expand radially as they stagnate against the plate. By  $1000 \mu\text{s}$  (1 ms), expansion of the sides of the test bed is evident. From Fig. 35, it is seen that by 75% of the impulse has been delivered to the plate by 1 ms. By 2 ms, for this charge and standoff, 90% of the impulse has been delivered. As mentioned in Section 2.2, there is a reflection off the bottom boundary of the computation (and in the experiment). In the 2-D cylindrical coordinates, there tends to be a focusing of waves on the centerline because of perfect cylindrical convergence. However, by 4 ms, the pressures have dissipated to a little over one atmosphere ( $10^5 \text{ Pa}$ , or  $10^6 \text{ dynes/cm}^2$ ). This justifies the use of  $\sim 4.75 \text{ ms}$  to compare the experimental data with simulation results (Figs. 35-37). By 6 ms, overpressures have completed dissipated, Fig. 39(h).

Expanded radial views of the material flow and associated pressure contours are shown in Fig. 40 at 1.0, 1.5, and 2.0 ms. It is observed that the vorticity associated with the radial flow of the soil and explosive products has resulted in the pressure field wrapping around the edges of the plate. As an aside, we have noticed that on occasion, these very large numerical eddies can result in a pushing “down” on the plate.

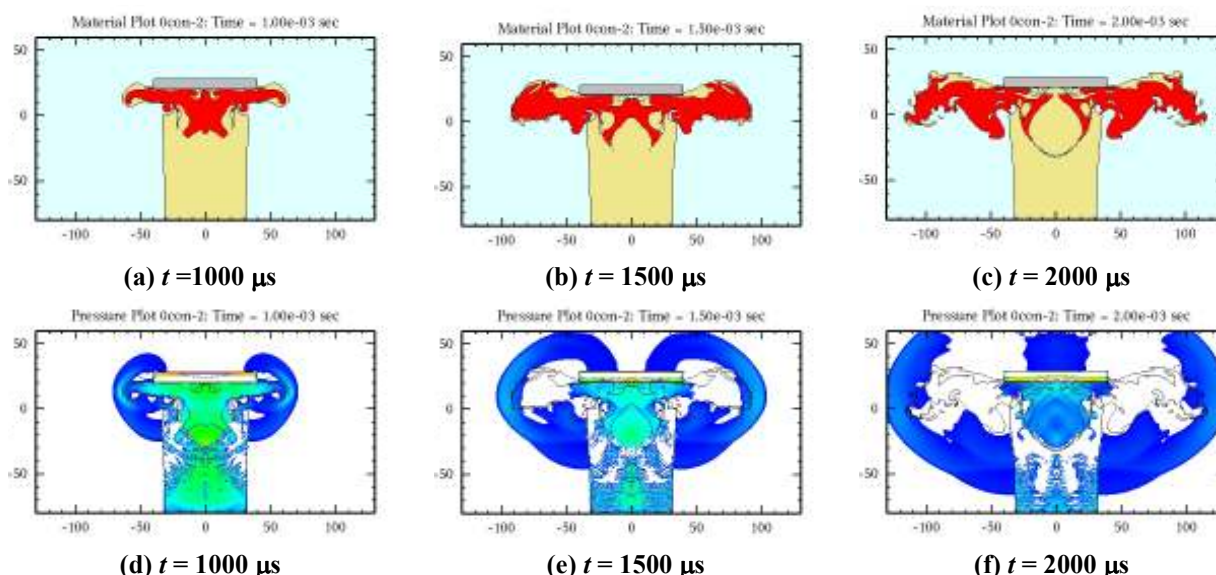


**Figure 40. Expanded view of select times after detonation for mine blast loading of flat plate.**

From Fig. 35, the plate has absorbed approximately 1500 kg-m/s of impulse by 1 ms. Since the plate is 300 kg, this means that the plate is moving at approximately 5 m/s at the end of 1 ms (the final velocity of the plate is approximately 7 m/s). However, loading does not begin until approximately 0.25 ms after explosive initiation. Assuming that the velocity profile is approximately linear from 0.25 ms to 1.0 ms, the average velocity of the plate over this time interval is then 2.5 m/s. Thus, the plate has moved slightly less than 2 mm during this loading time. Therefore, the assumption of impulsive loading—that the structure does not have time to move during loading—is a very good approximation for these experiments.

#### 4.6.2 Effect of EOS, Including Initial Density

Several parametric studies were conducted to investigate the influence of some of the parameters used in the simulations. These investigations were performed using the 2-D cylindrically symmetric option of CTH (with an increased plate thickness to have a 300-kg mass plate, see Section 4.5). A number of investigators have reported that the momentum transferred to a plate depends strongly on initial soil density [22,28,29,33]. The initial soil density as a function of moisture content for the various default sand EOS's in CTH (Table 6) is shown in Fig. 41. It is seen that initial density is approximately linear with moisture content.

However, prior to showing the effect of initial moisture content, a decision had to be made concerning which EOS to use for the 7% moisture content of the experiments. Tabular EOS's for moisture contents of 6% and 8% exist in CTH (see Section 4.2 and Table 6). To remove the issue of initial density, the two EOS's were run with the same initial density as the experiments ( $1.37 \text{ g/cm}^3$ ). Plate momentums versus time are shown in Fig. 42. Plate momentums are identical within numerical uncertainties. Next, a simulation was conducted using the 6% moisture content EOS, but with the default density of CTH. These results are also shown in



Fig. 42. It is clearly seen that initial soil density, all other things being equal, has a significant effect on the momentum transferred to the plate. Thus, we conclude, at least for sand-type soils, the primary effect of moisture content is to change the initial density, and it is very important to get this parameter correct for accurate simulations.

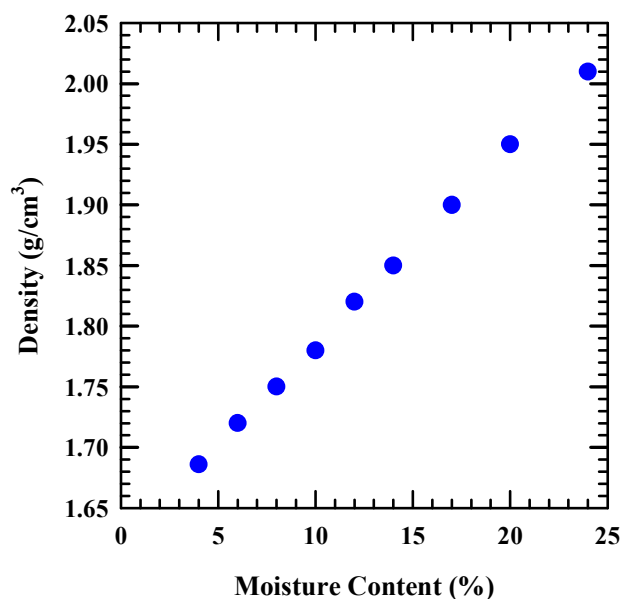


Figure 41. Initial soil density vs. moisture content (default values in CTH).

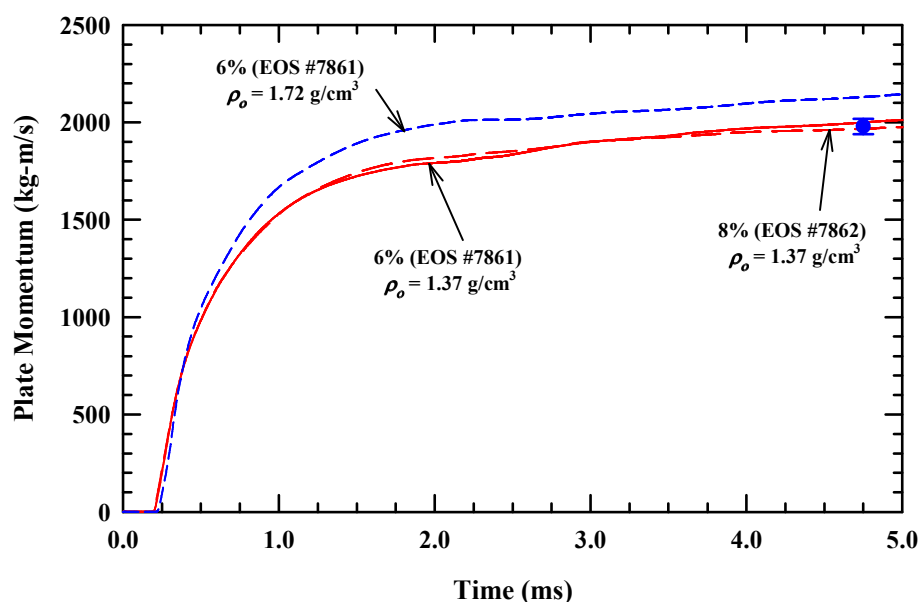


Figure 42. Plate momentum vs. time for various EOS's.

#### 4.6.3 Effect of Charge Mass

It was noted previously that the charge (HE) mass for the experiments was 625 g, but that an HE mass of 637 g was used in the simulations. The 637 g of HE preserved the height-to-diameter ratio of 1/3, and also accounted for the ~10 g of PETN in the booster (initiator). It was decided to investigate the influence of small decreases in the mass of the HE: 2.5% (621 g), 5% (605g), and 7.5% (589 g). The results are shown in Fig. 43 for the 20-cm standoff and Fig. 44

for the 30-cm standoff. The charge mass was changed by decreasing the thickness of the explosive, while keeping the top of the explosive 5 cm below the surface of the sand. The change in final plate momentum is  $\sim 0.9\%$  for each 1% decrease in HE mass at the 20-cm standoff, and  $\sim 0.75\%$  for each 1% decrease in HE mass at the 30-cm standoff. As noted previously, there is some variability in final plate momentums at late times due to the formation of the large (computational) eddy structures as the sand and explosive products expand radially after stagnating against the flat plate. However, it is noted that changing the HE mass by only 2.5% results in a change in the plate momentum comparable to the repeatability of the experiments at the 20-cm standoff.

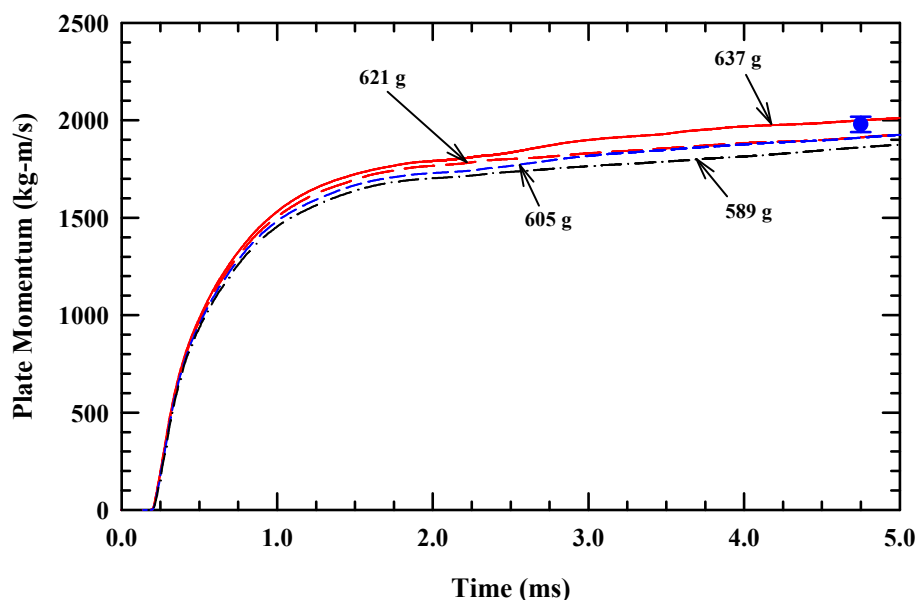


Figure 43. Effect of HE mass on plate momentum: 20-cm standoff (2-D).

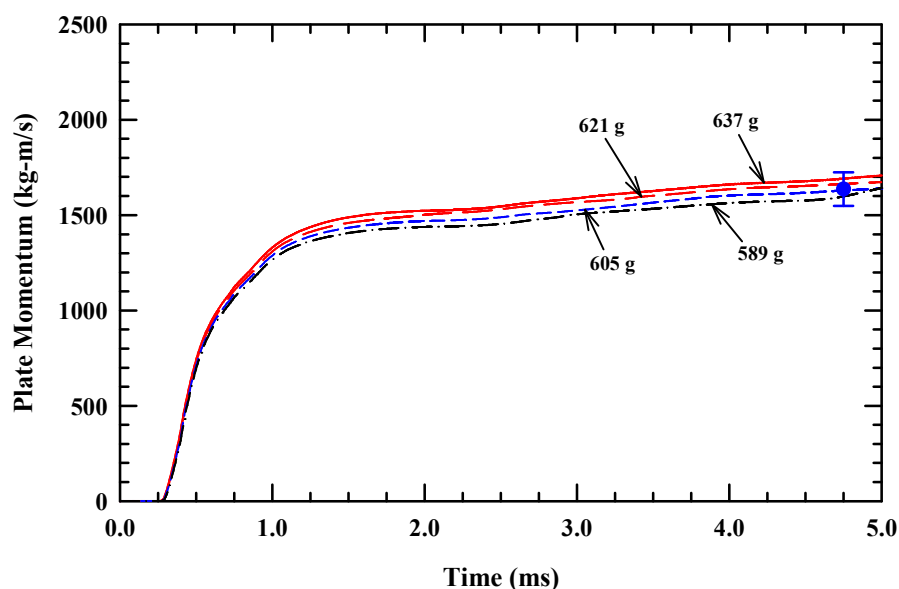


Figure 44. Effect of HE mass on plate momentum: 30-cm standoff (2-D).

#### 4.6.4 Effect of Soil Strength

The next parametric study conducted was to examine the effect of soil strength. The soil strength model is given by Eqn. (11). An initial set of runs examined the influence of  $Y_{max}$ . The value of  $Y_{max}$  was changed from the nominal 160 MPa to 320 MPa (double strength), 80 MPa (half strength), and then zero strength, i.e., a hydrodynamic sand. The results are shown in Fig. 45. It is seen that doubling or halving the value of  $Y_{max}$  has only a very small effect on the momentum transferred to the plate. In fact, the effect of these changes in  $Y_{max}$  or strength cap can probably be considered to be within numerical accuracy (considering variations in results due to zone size; see for example, Fig. 35). The parameter  $\beta$  was also varied; values of 1.5, 2.0 (nominal), and 2.5 were used, with  $Y_{max}$  held constant at 160 MPa. The plate momentum increased by less than 5% for  $\beta = 1.5$ , and decreased  $\sim 2.5\%$  for  $\beta = 2.5$ .

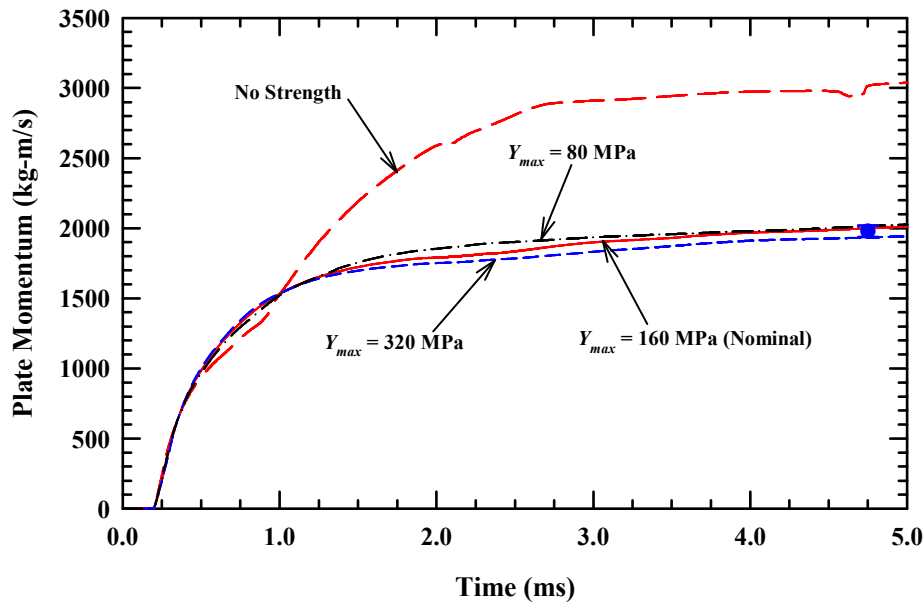


Figure 45. Parametric study on strength of soil.

In contrast to the aforementioned strength modifications, zero soil strength has a profound effect on the momentum transferred to the plate, increasing the momentum transferred by approximately 50%. As Kerley noted when he examined the effect of soil strength [33], the zero strength for the soil allows more ejection of the soil in the vertical direction, reducing the lateral expansion. The initial loading ( $\sim 0.25$  ms) from the zero-strength soil is essentially the same, but then the effect of increased loading over the area of the plate greatly increases the later-time momentum transfer to the plate.

As previously mentioned, Taylor, et al. [18], noted that impact of the soil cap is followed by impact of crater ejecta as the crater grows. The second phase of loading is dominated by processes associated with the excavation of a crater, and occurs over a much longer time and larger plate area than the first phase. It is seen in Fig. 45 that the larger impulse that results from the no-strength sand occurs during this second phase of loading, and is consistent with the observations of Kerley [29].

What is also noteworthy is that the effect of soil strength ( $Y_{max}$ ) is highly nonlinear. The momentum transferred for “half-strength” soil does not fall halfway between zero-strength and 160-MPa strength soil. From a modeling perspective, it is only necessary to have an approximate estimate for the strength, and simulation results will be quite insensitive to errors in

soil strength (at least for sand and the range of parameters investigated). Comparison of Fig. 45 with Fig. 42 shows that it is much more important to have an estimate of the correct initial soil density than soil strength.

#### 4.6.5 3-D Simulations: Effect of Moisture Content

A series of 3-D simulations was conducted to compare the momentum transferred to the flat plate as a function of soil moisture content. One plane of symmetry was used, with a zone size of 1.0 cm (cubic zoning throughout the computational grid). The computational plate momentum was converted to jump velocity by dividing by the plate mass. The results, as a function of moisture content, are plotted and compared to the experiments in Fig. 46. The computational jump velocity results tend to be slightly higher than the averaged experimental results; but, in general, the simulation results lie within two standard deviations of the averaged experimental results.

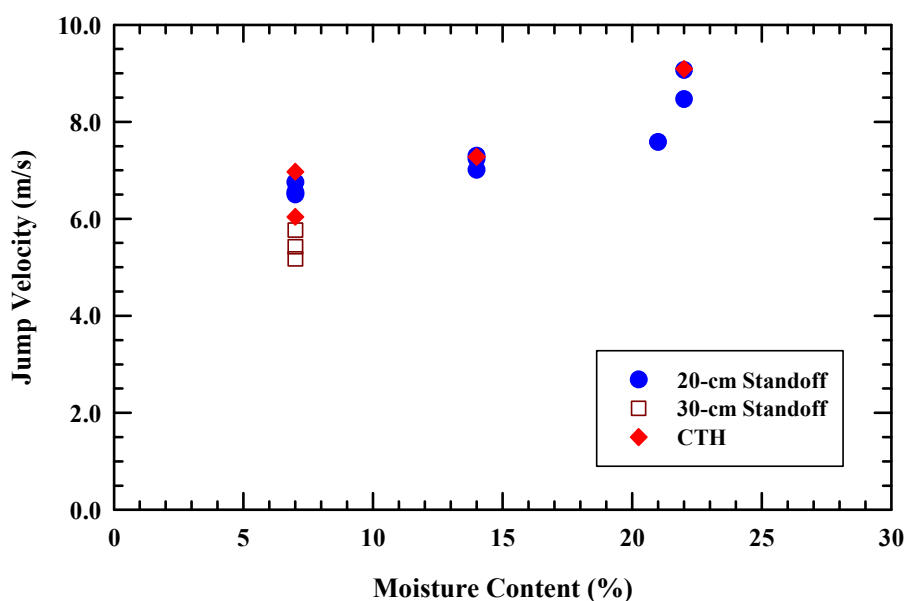


**Figure 46. Comparison of 3-D simulation results to flat-plate experiment: jump velocity vs. soil moisture content.**

One possible difference between the simulations and the experiments is that the simulations assumed a perfectly reflective boundary at the base of the test bed; whereas in the experiments, some of the downward propagating shock is transmitted. This effect would lower the reflected pressure from the bottom test bed boundary, and slightly decrease the final momentum transferred to the plate. On the other hand, the simulations do not model the low-strength, cardboard Sonotube, which had to be replaced after each test. At some point, given the number of approximations that are made in material modeling, mesh resolution, numerical uncertainties, etc., it is probably misleading to “tweak” constants used in the simulations to achieve better agreement with the experiments than already obtained.

#### 4.6.6 Summary of Flat-Plate Simulations

It has been demonstrated that, in general, numerical simulations can reproduce the results of loading of flat plates from mine blasts within the scatter of experiments. Results were compared for three different moisture contents and two standoff distances. The metric for comparison was the momentum transferred to the plate, or alternatively, the plate jump velocity. It was

demonstrated that it was very important to have the initial sand density correct in the simulations for accurate predictions.

## 4.7 V-Shaped Plates

### 4.7.1 V-Shaped Plate: 3-D Results

Simulations, using the 1-cm cubic zone size, were performed for the V-shaped plates. Results are shown in Fig. 47. The experimental results—for the four sets of experiments that were conducted with the nominal 7% moisture content—are shown with the vertical bars, along with two standard deviations about the experimental average. The simulation results are denoted by the diamonds. As previously mentioned with respect to simulating the flat-plate experiments, the simulation results lay within 2 standard deviations of the average. However, the simulations greatly overpredict momentum transfer to the V-shaped plates, although the trend is in the correct direction.

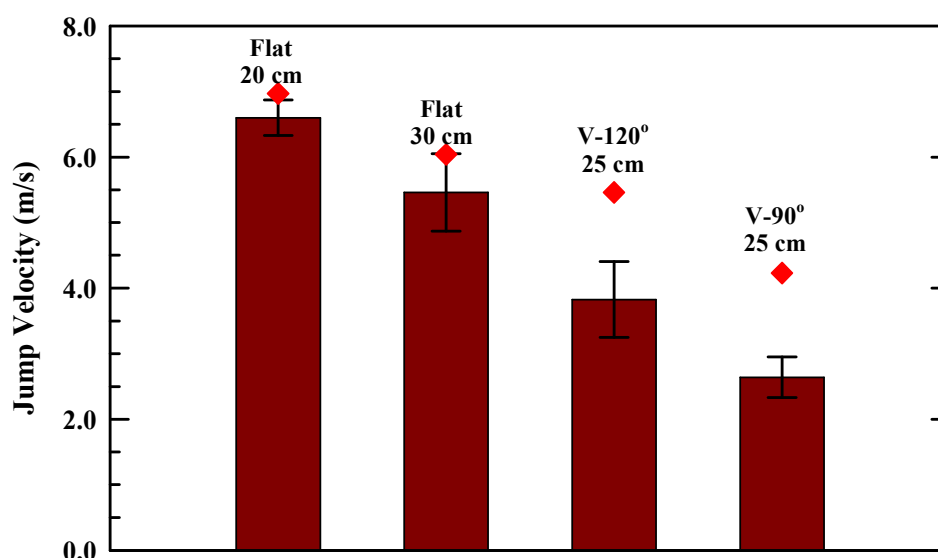


**Figure 47. Jump velocity vs. plate type: 3-D simulations and experimental results.**

Several things were tried to improve the predictions of the simulations. The V-shaped geometry results in the plate cutting through the computational grid at an angle, and thus there are many mixed cells that contain the steel plate and other constituents such as air, explosive products, and sand. It was not clear how best to treat “strength” in these mixed cells. It will be shown in Section 4.7.2 that computational results were relatively independent of the various ways to treat mixed cell strength.

It was decided to refine the computational grid, so simulations were performed with a mesh size of 0.5 cm. Results for the 90° and 120° V-shaped plates are shown in Fig. 48. There is significant reduction in momentum transfer to the plates as mesh resolution increased (as zone size decreased). However, going to smaller zones was computationally prohibitive as will be discussed in Section 4.7.3.

It has been demonstrated for flat plates, where the loading for the mine blast stagnates against the plate, that the simulations can accurately predict the momentum transferred provided that the properties of the soil are represented reasonably accurately. The fact that the calculated

momentum is too large for the V-shaped plates suggests that, somehow, the flow of material along the plate is coupling too much energy (momentum) to the plate. In the next subsection, various things were tried to see if better agreement could be obtained between simulations and experiments for the V-shaped plates.

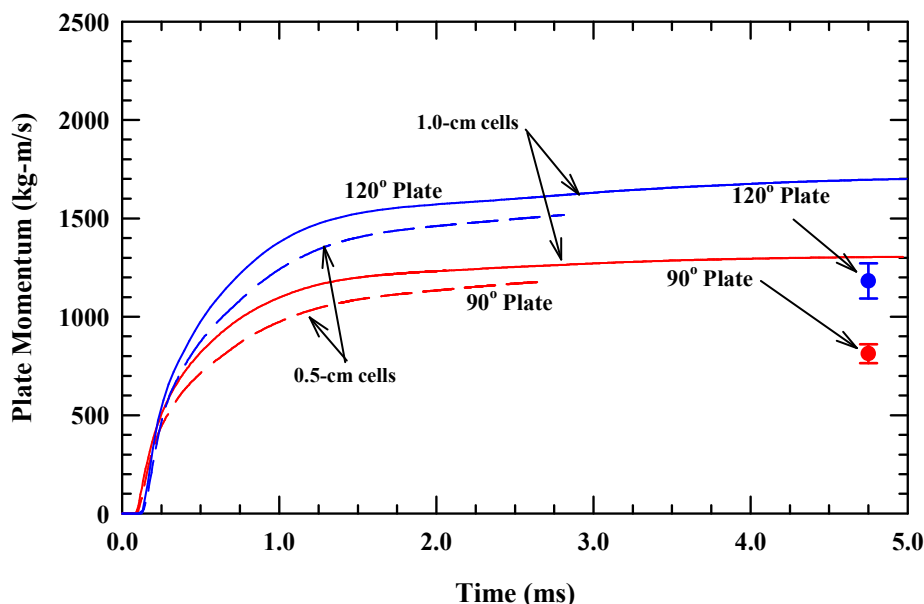


Figure 48. Plate momentum vs. time for V-shaped plates: 3-D simulations.

#### 4.7.2 V-Shaped (Conical) Plates: 2-D Results

When it was realized that there were issues with the V-shaped plates, it was decided to generate a two-dimensional analogue that would permit parametric studies more readily. Since the loading from the buried HE charge is predominantly focused in the region above the mine, it was decided to make a conical plate, with the correct thickness, as a 2-D surrogate of the V-shaped plate. The conical plates shown here maintain a similar thickness and width to the V-shaped plates. However, it is noted that the geometry of conical plate, although similar in a cross-sectional view, is not the same as a V-shaped plate. The mass of the conical plate is less than that (approximately one half) of the V-shaped wedge plate.<sup>5</sup> The V-shaped plate is a wedge; thus, in the plane perpendicular to the V-shape, the bottom of the wedge is at a constant distance above the soil test bed. Therefore, loading from the mine blast is larger on the V-shaped wedge as compared to the conical plate. Nevertheless, it is expected that trends in simulated results would be the same for the conical plate as for the V-shaped wedge plate.

One explanation postulated for the inaccurate prediction of momentum transferred to the V-shaped plates was that the flow along the boundary of the plate was somehow being impeded by the treatment of strength in mix cells, thereby imparting more momentum to the plate. That is, the mine blast products were not flowing along the solid plate boundary in the simulations as freely as they should.<sup>6</sup> In particular, the V-shaped plate cuts through the rectangular-oriented

<sup>5</sup> Additional simulations were performed using a modified conical plates with a mass of 300 kg, and the results varied less than ~5%. The momentum transferred to the plates is very similar, although the final plate velocities are different because of differences in plate mass.

<sup>6</sup> It was recognized that mixed cells did not seem to present a problem for stagnating flow on the flat plate, where the mine blast debris had to turn and flow parallel to the plate. For the V-shaped plate, the flow is also parallel to the plate, but there is no stagnation of the—in this case—vertical component of the velocity.

grid at an angle. Clearly there are many mixed cells of steel and mine blast products. Therefore, it was decided to investigate various assumptions for the treatment of mixed cell strength: 1) the strength is the volume weighted average of the materials in the cell (Mix = 1); 2) strength is a volume weighted average of the materials that can support shear (Mix = 3, the usual default), and 3) no strength (Mix = 5). Results are shown in Fig. 49 for two different grid resolutions.<sup>7</sup> Although there are differences in the final plate momentum as a function of zone size (1.0-cm and 0.5-cm zones), little difference exists between the various treatments of strength in mixed cells.

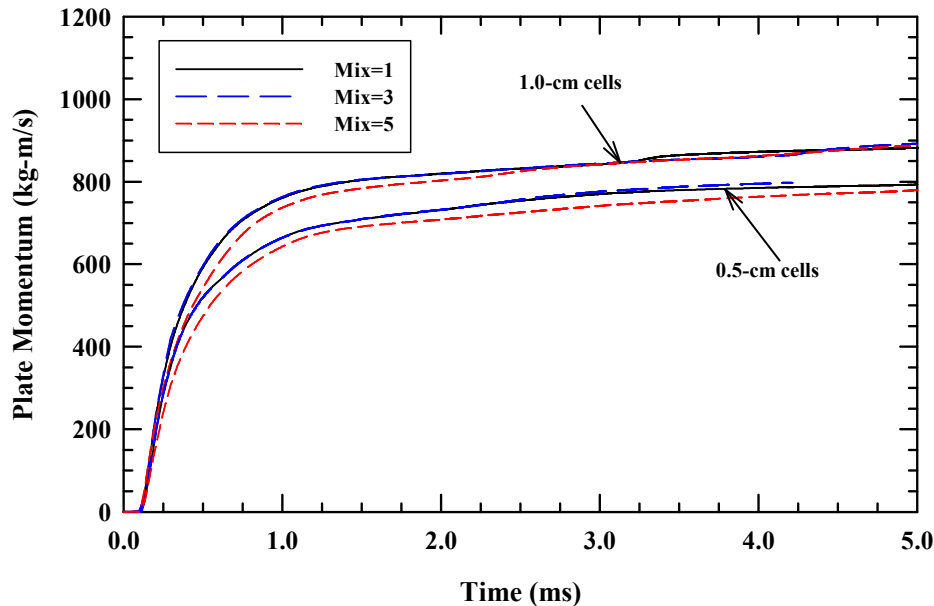


**Figure 49. Plate momentum (90°-conical plate) as a function of treatment of mixed cells.**

At this point, since there was a relatively large difference in the final plate momentum between the 1.0-cm and 0.50-cm zone size (Figs. 48 and 49), it was decided to conduct a zoning study of the two V-shaped conical plates. The results for the 90° plate are shown in Fig. 50 for zone sizes ranging from 2.5-cm cells to 0.125-cm cells (all cells were “square”). It appears that the computational results are slowly converging, but even with 0.125-cm zones, the simulations may not be fully converged. In contrast to the flat-plate convergence study, convergence is asymptotic from one direction: momentum transfer to the plate decreases as the mesh resolution increases (zone size decreases).

Material plots are quite revealing as to the underlying mechanics. Material plots, all at 1 ms, are shown in Fig. 51 for 5 different mesh sizes. The Richtmyer-Meshkov Instability (RMI) [18], as resolved by the interface tracking algorithm, results in a turbulent-like flow past the plate for the finer grid resolutions. The simulations, of course, are calculating a turbulent-like flow field characterized by small-scale vorticity (eddy structures) only at grid resolutions where numerical

<sup>7</sup> Note that the plate momentum for the conical plate is approximately 30% less than that for the V-shaped wedge plate, Figs. 48 and 49. The experimental data points for the V-shaped plates are not placed on the graphs with the conical plate results since the plate geometries are different.

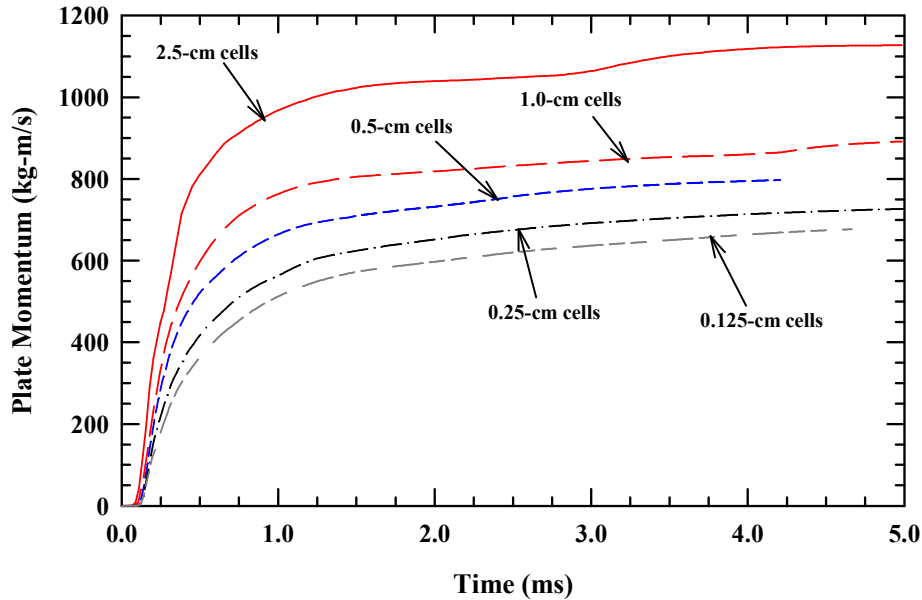


**Figure 50. Plate momentum for 90°-conical plate as a function of zone size (2-D).**

diffusion is not smearing out velocity gradients and material gradients in the flow field. In Fig. 51, at the coarser grid resolutions (2.5-cm and 1.0-cm), numerical diffusion from the 2nd-order advection scheme does not allow for prediction of any fine scale structure to the explosive products (red color) and soil (yellow color). However, as the grid is refined (grid resolutions of 0.25-cm and 0.125-cm), and numerical diffusion is reduced, then velocity and material gradients are maintained such that vorticity may develop (rotation of fluid elements, the curl of the velocity field) and thus fine scale turbulent-like flow structures develop and are resolved. We refer to these flow structures as turbulent-like, because they lack one key attribute essential to true turbulent flows: these turbulent-like flows are not dissipative. Aside from shock viscosity, there are no traditional fluid viscous forces (Reynolds stresses) [41-43] included in the formulation for most hydrocodes. Thus, there are no viscous stress terms in either the momentum or energy equations and it is these terms that model dissipative processes in fluids. However, the primary driver to accurately modeling the loads on the plate is the characteristic structure of the interaction of the mine blast products with the plate. That is, a coarsely resolved flow field tends to allow the mine blast products to form a more coherent (integral) large-scale flow structure that more uniformly interacts with the plate, e.g., see Fig 51(a). At finer resolutions, the mine blast products are less coherent due to the increased vorticity being generated and result in more localized loading on the plate by eddy flow structures, as shown in Fig. 51(e). This latter effect is physically consistent for these types of flow fields and results in less momentum transferred to the plate as confirmed by the experiments.

The convergence study for the 120° conical plate is shown in Fig. 52. Convergence is again asymptotic from one direction; however, convergence appears to be occurring more rapidly for the 120° conical plate than for the steeper, 90° conical plate. Nevertheless, convergence has not been achieved/demonstrated.



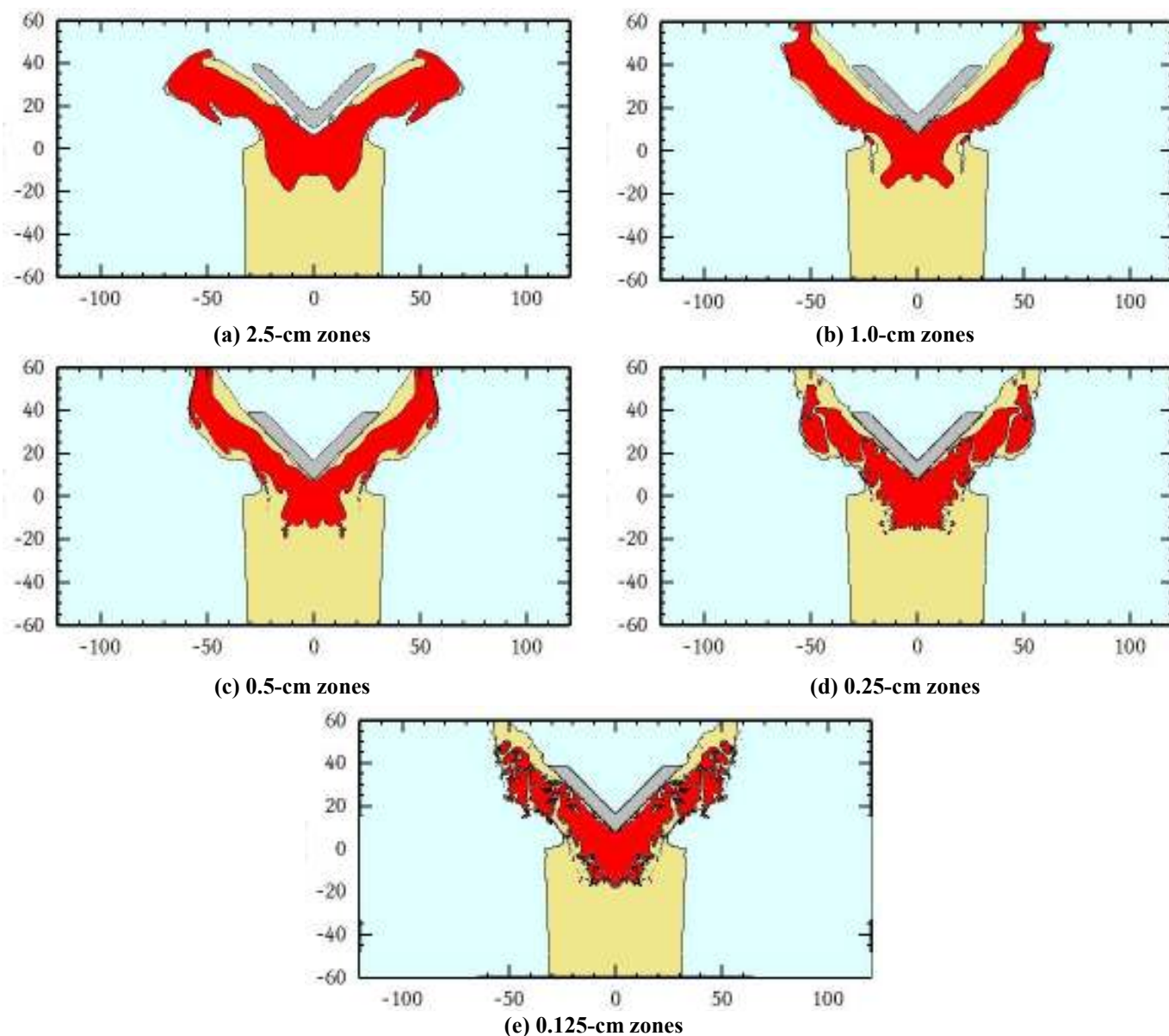


**Figure 51. Material plots showing loading of 90° V-shaped conical plate at 1.0 ms.**

It is unknown if further refinement of the computational grid will provide a converged result that matches the experimental data. The trend appears to be in the correct direction. We speculate that with a sufficiently refined grid, which resolves the relevant length scale of the turbulent flow, that the loading to the plate would be correct. Dissipation of energy in the turbulent flow—not modeled because of the absence of the Reynolds stresses in the momentum and energy equations—would be a second-order effect. However, this is an area for future research.

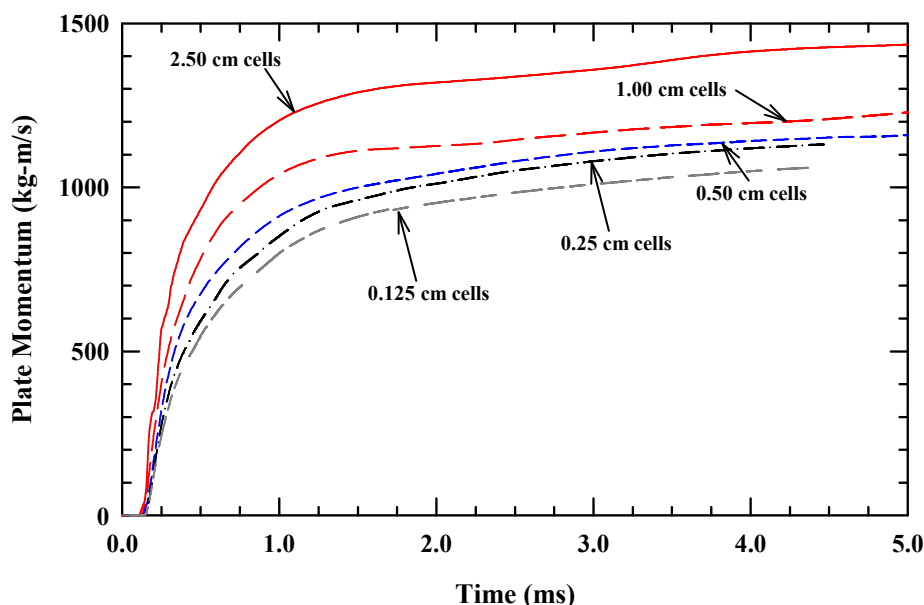


Figure 52. Plate momentum for 120°-conical plate as a function of zone size.

### 4.7.3 V-Shaped Plates: Summary

The V-shaped plates provide a computational challenge for simulating mine blast loading accurately. The 3-D simulations, using 8 (2<sup>+</sup>-GHz) processors, were typically taking ~96 hours to run to approximately 5 ms using the 1-cm zone size.<sup>8</sup> Decreasing the zone size by half, and not adding additional processors, would require 1536 hours of wall-clock time. Adding additional processors can reduce the run time; however, using 128 (16 x 8) processors does not reduce the run time back to ~96 hours because of computational overhead required for processors to exchange information at the boundary of their domains. Further, the simulations are not converged with 0.5-cm zones, so a numerical solution potentially requires even (considerably) more computational resources.

The simulations overpredict the momentum transferred to the V-shaped plate; and therefore, from a design perspective, any mitigating designs based on these results would be conservative. However, they also would tend to be heavier than necessary. A possible approach is to implement an analytical loading function that provides the correct loading as a function of distance for a flat plate (for appropriate soil moisture content), and see if this analytic function can be used to load the V-shaped plate. This, of course, would need to be demonstrated.

## 4.8 3-D Flat-Plate Simulations Revisited

It was decided to do one last set of simulations in 3-D to ensure that the conclusions of the charge mass parametric studies in two dimensions were valid. The charge mass was varied systematically for the 20-cm and the 30-cm standoffs. As done for the 2-D cylindrically symmetric simulations (Section 4.6.3), the charge mass was changed by increasing or decreasing

<sup>8</sup> The flat-plate simulations were run with one plane of symmetry that halved the problem size. However, we found that we could not make use of the plane of symmetry for the V-shaped plate because of an error associated with the boundary condition on the supposed plane of symmetry. The root cause of this problem was not investigated further, but the consequence was that the number of computational zones, and hence run time, doubled for the V-shaped plates.

the thickness of the explosive, while maintaining the depth of burial as 5 cm (from the top of the explosive to the soil surface). Results for the 20-cm standoff are shown in Fig. 53. It is seen that the 625-g charge result agrees better with the experiment than the 637-g result (which accounts for the explosive in the detonator). Similarly, the result for the 625-g charge provides better agreement with the experimental data than the 637-g charge for the 30-cm standoff, Fig. 54. It may be that the effect of the booster charge, which is centered at the bottom of the main

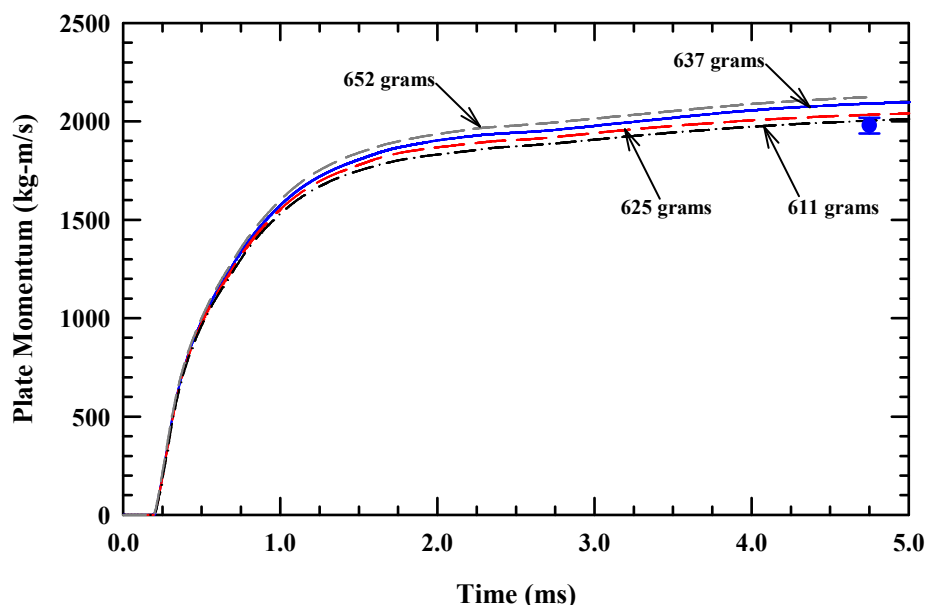


Figure 53. Effect of HE mass on flat-plate momentum: 20-cm standoff (3-D).

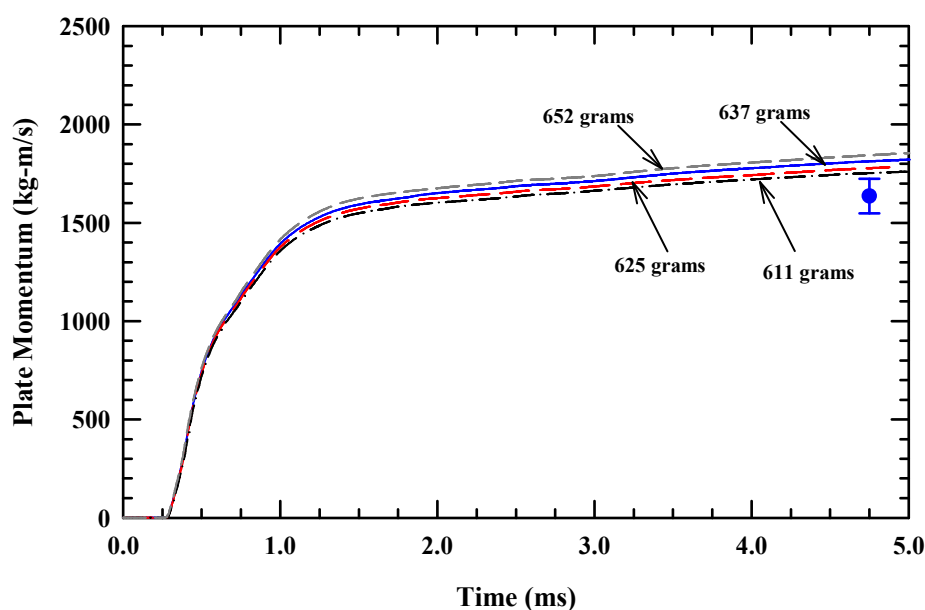


Figure 54. Effect of HE mass on flat-plate momentum: 30-cm standoff (3-D).

explosive charge, is not an “additive effect”. However, before too much credence is given to the simulation results, it is noted that the difference between the 637-g and 625-g simulations is only 2% to 3%, which is probably smaller than the overall accuracy of the simulations (3% to 5%, see

Fig. 37). Further, the “error” bars on the experimental data represent one standard deviation of the experimental results (of a very limited number of experiments) about the average (plotted as the circle). The simulation results, regardless of whether 625-g or 637-g of explosive is used, lie within 2 standard deviations of the data; and, at best, we can only expect the simulations to reproduce the experiments within experimental scatter. Additionally, assumptions were made about the equation of state for the soil, which then has its own inherent approximations.

Thus, we are very pleased with the results of the 3-D flat-plate simulations, which reproduce the experimental data within data scatter. We caution that small changes in input parameters that provide better agreement with the experimental data may be real, or they may simply be fortuitous given constitutive assumptions and the accuracy of the numerical hydrodynamics.

## 5.0 Summary and Conclusions

Mine blast loading experiments were designed and conducted. The experiments were designed to investigate loading as a function of soil moisture content, plate standoff, and plate shape. Three experiments were conducted for each test condition to provide an indication of the variability of response for nominally identical experiments. Total momentum transferred to the plate, as measured by the maximum height the plate traveled, was the primary experimental metric. The maximum height permitted a calculation of the jump velocity, which along with plate mass, gave the momentum transferred to the plate from the mine blast loading. It was found that soil density increased with moisture content, as did momentum transfer to the plate. A 22% increase in soil density resulted in a 27% increase in the momentum transferred to a flat plate. A 50% increase in plate standoff (20 cm to 30 cm), at the same moisture condition, resulted in a 17% decrease in momentum transfer.

The momentum transferred from the mine blast was greatly reduced for the V-shaped plates. The center of mass of the V-shaped plates was placed at 25 cm above the top of the test bed. Momentum transfer was reduced, compared to the 20-cm-standoff flat plate, by 40% for the 120° V-shaped plate and 60% for the 90° V-shaped plate. Of course, the V-shaped plates require higher center of gravities.

Numerical simulations of the experiments were conducted. The equation of state for sand, as implemented into CTH, as a function of initial porosity and moisture content was summarized. It was demonstrated that the initial density of the sand is very important for obtaining good agreement between simulations and experimental results. It was also demonstrated that it is important to account for the strength of sand, but that once taken into account, fairly large changes (from -50% to +100% for the cap,  $80 \text{ MPa} \leq Y_{max} \leq 320 \text{ MPa}$ ) in strength had little effect on momentum transfer.

Grid convergence studies showed, for flat-plate response, that numerical convergence and good agreement with the experimental data could be obtained with a reasonable mesh/zoning size, i.e., the HE charge was resolved with approximately 11 zones across the diameter and just under 4 zones through the thickness. These simulations reproduced, within experimental scatter, the momentum transfer results for the flat-plate experiments (two plate standoff distances and three soil moisture contents at one of those standoff distances).

Simulations of the V-shaped plate experiments were not as accurate, however. Even with a computational mesh with 8 times the resolution of the flat-plate simulations, numerical convergence still had not been achieved for the 90° V-shaped plate, although there was an indication that 2 to 4 times the flat-plate resolution might provide reasonable numerical convergence for the 120° V-shaped plate.<sup>9</sup> The difficulty in achieving numerical convergence is attributed to the generation of numerical turbulent-like flow along the plate, triggered by the Richtmyer-Meskov instability. Since there are no Reynolds viscous stress terms in the momentum and energy equations, the coarsely resolved flow field overpredicts the interaction of the mine blast products with the angled plate. Using the same mesh resolution as for the flat plate simulations, the simulations overpredict the momentum transferred to the 90° plate by approximately 61% and to the 120° plate by 43%. From an armor design perspective, the overprediction provides an additional safety margin since the calculated loads are too high. However, the potential weight savings that would be provided by the V-shaped plate would not

---

<sup>9</sup> Numerical convergence was determined from 2-D axisymmetric simulations of a conical plate.

all be realized. Experimentally, the 120° and 90° plates reduce the momentum transferred by 40% and 60%, respectively; the simulations predict only a 17% and 36% reduction, respectively, for the two V-shaped plates (compared to the 20-cm-standoff flat plate). But it was also shown that with sufficient mesh resolution, the numerical mine blast products are less coherent; thus, loading to the plate is more physically localized. Perhaps with sufficient computational resources, accurate analyses of the V-shaped plates could be realized, but this is clearly an area of future research.

## **6.0 Acknowledgements**

The authors thank Dr. Chris Freitas of Southwest Research Institute for insightful discussions concerning zone-size effects associated with large-scale turbulence. The authors thank Mr. Trent Kirchdoerfer for assistance in some early calculations and providing support in the EOS studies, and Mr. Dick Sharron for his assistance in the conduct of many of the parametric studies and 3-D simulations.

UNCLASSIFIED



## 7.0 References

1. P. S. Westine, B. L. Morris, P. A. Cox, and E. Z. Polch, "Development of computer program for floor plate response from land mine explosions," R&D Center Laboratory Tech Report 13045, U.S. Army Tank-Automotive Command Research and Development Center, Warren, MI (1985).
2. L. Laine, Ø. Ranestad, A. Sadnvik, and A. Snekkevik, "Numerical simulations of anti-tank mine detonations," *Shock Compression of Condensed Matter – 2001* (M. D. Furnish, N. N. Thadhani, and Y. Horie, Eds.), AIP CP 620, pp. 431-434, American Institute of Physics, Melville, NY (2002).
3. A. G. Mikhail, "Off-center explosion of blast land mine under ground vehicles: variation in lethality," *Proc. 21<sup>st</sup> Int. Symp. Ballistics* (N. Burman, J. Anderson, and G. Karselis, Eds.), **2**: 1058-1069, Defense Science and Technology Organisation, Adelaide, Australia (2004).
4. B. Zakrisson, B. Wikman, and B. Johansson, "Half scale experiments with rig for measuring structural deformation and impulse transfer from land mines," *Proc. 24<sup>th</sup> Int. Symp. Ballistics* (S. Bless and J. Walker, Eds.), **1**: 497-504, DEStech Publications, Inc., Lancaster, PA (2008).
5. S. Peles, D. Touati, I. Azulay, and A. Neuberger, "Numerical simulation of mine detonation beneath a generalized add-on armor structure," *Proc. 24<sup>th</sup> Int. Symp. Ballistics* (S. Bless and J. Walker, Eds.), **1**: 439-447, DEStech Publications, Inc., Lancaster, PA (2008).
6. M. Held, P. Heeger, and J. Kiermeir, "Displacement device to measure the acceleration of the bulge of THA plates under anti-tank mine blast," *Proc. 22<sup>nd</sup> Int. Symp. Ballistics* (W. Fliss and B. Scott, Eds.), **2**: 995-1000, DEStech Publications, Inc., Lancaster, PA (2005).
7. R. R. Skaggs, J. Watson, T. Adkins, W. Gault, A. Canami, and A. D. Gupta, "Blast loading measurements by the vertical impulse measurement fixture (VIMF)," ARL-TR-3383, Army Research Laboratory, Aberdeen Proving Ground, MD (2004).
8. R. R. Skaggs, W. Gault, and L. C. Taylor, "Vertical impulse measurements of mine buried in saturated sand," ARL-TN-250, Army Research Laboratory, Aberdeen Proving Ground, MD, Jan. (2006).
9. A. D. Gupta, R. R. Skaggs, J. Watson, T. Adkins, W. Gault, A. Canami, and N. Gniazdowski, "Comparison and validation of computational blast loadings with experiment," ARL-TR-3219, Army Research Laboratory, Aberdeen Proving Ground, MD, June (2004).
10. D. A. Cendón, F. Gálvez, A. Enfedaque, and V. Sánchez-Gálvez, "Analysis of armoured vehicles blast protection by using finite element codes," *Proc. 23<sup>rd</sup> Int. Symp. Ballistics* (F. Gálvez and V. Sánchez-Gálvez, Eds.), **2**: 843-852, Gráficas Couche, S.L., Madrid (2007).
11. R. Colbert, M. Majerus, and W. Clark, "Challenges and a solution in determining land mine or IED neutralization effectiveness," *Proc. 22<sup>nd</sup> Int. Symp. Ballistics* (W. Fliss and B. Scott, Eds.), **2**: 1381-1388, DEStech Publications, Inc., Lancaster, PA (2005).
12. P. Gaudreault, A. Bouamoul, R. Durocher, and B. St-Jean, "Finite element modeling of light armoured vehicle welds heat affect zone subjected to an anti-vehicular blast landmine, a summary of the numerical model and field experiments," *Proc. 22<sup>nd</sup> Int. Symp. Ballistics* (W. Fliss and B. Scott, Eds.), **2**: 1079-1085, DEStech Publications, Inc., Lancaster, PA (2005).
13. S. Hlady, D. Bergeron, and R. Gonzalez, "Protecting vehicles from landmine blast," *Proc. 22<sup>nd</sup> Int. Symp. Ballistics* (W. Fliss and B. Scott, Eds.), **2**: 1239-1246, DEStech Publications, Inc., Lancaster, PA (2005).
14. S. Rolc, J. Buchar, J. Kratky, R. Graeber, M. Havlicek, and J. Perchacek, "Response of the plate to the buried blast mine explosion," *Proc. 24<sup>th</sup> Int. Symp. Ballistics* (S. Bless and J. Walker, Eds.), **1**: 512-519, DEStech Publications, Inc., Lancaster, PA (2008).

15. J. Motuz, D. S. Cronin, M. Worswick, D. Bourget, K. Williams, and G. Pageau, "Numerical modeling of a simplified surrogate leg subject to an anti-personnel blast mine," *Proc. 19<sup>th</sup> Int. Symp. Ballistics* (E. R. Crewther, Ed.), **2**: 913-919, Interlaken, Switzerland, 7-11 May (2001).
16. A. G. Mikhail, "Vulnerability of light ground vehicles and their crews to acceleration resulting from battlefield threats," *Proc. 20<sup>th</sup> Int. Symp. Ballistics* (J. Carleone and D. Orphal, Eds.), **2**: 1252-1263, DEStech Publications, Inc., Lancaster, PA (2002).
17. D. A. Cendón, V. Sánchez-Gálvez, F. Gálvez, and A. Enfedaque, "The use of foam structures in armoured vehicle protection against landmines," *Proc. 22<sup>nd</sup> Int. Symp. Ballistics* (W. Fliss and B. Scott, Eds.), **2**: 1048-1055, DEStech Publications, Inc., Lancaster, PA (2005).
18. L. C. Taylor, W. L. Fourney, U. Leiste, and B. Cheeseman, "Loading mechanism on a target from detonation of a buried charge," *Proc. 24<sup>th</sup> Int. Symp. Ballistics* (S. Bless and J. Walker, Eds.), **2**: 975-983, DEStech Publications, Inc., Lancaster, PA (2008).
19. A. Bouamoul and G. Toussaint, "Experimental tests and numerical calculations using ALE and SPH approaches on mine blast effects on structure," *Proc. 24<sup>th</sup> Int. Symp. Ballistics* (S. Bless and J. Walker, Eds.), **1**: 535-539, DEStech Publications, Inc., Lancaster, PA (2008).
20. A. Neuberger, S. Peles, and D. Rittel, "Scaling the response of circular plates subjected to large and close-range spherical explosions. Part II: Buried charges," *Int. J. Impact Engng.*, **34**(5): 874-882 (2007).
21. A. Neuberger, S. Peles, and D. Rittel, "Scaling the response of circular plates subjected to large and close-range spherical explosions. Part I: Air-blast loading," *Int. J. Impact Engng.*, **34**(5): 859-873 (2007).
22. N. Heider and A. Klomfass, "Numerical and experimental analysis of the detonation of sand-buried mine," *Proc. 22<sup>nd</sup> Int. Symp. Ballistics*, **2**: 1389-1396, DEStech Publications, Inc., Lancaster, PA (2005).
23. Moxnes, J. F., G. Ødegårdstuen, A. Atwood, and P. Curran, "Mechanical properties of a porous material studied in a high speed piston driven compaction experiment," *30<sup>th</sup> Int. Annual Conf of ICT*, Karlsruhe, Germany, June 29 – July 2 (1999).
24. L. Laine, "Numerical simulations of ground shock attenuation layers for Swedish rescue centres and shelters," *4<sup>th</sup> Asia-Pacific Conf on Shock and Impact Loads on Structures*, CI-Premier PTE, Ltd., Sinapore, Nov (2001).
25. M. Grujicic, B. Pandurangan, Y. Huang, B. A. Cheeseman, W. N. Roy, and R. R. Skaggs, "Impulse loading resulting from shallow buried explosives in water-saturated sand," *J. Materials: Design and Applications*, **221**: 21-35 (2007).
26. M. Grujicic, B. Pandurangan, and B. A. Cheeseman, "A computational analysis of detonation of buried mines," *Multidiscipline Modeling in Mat. and Stru.*, **2**: 363-387 (2006).
27. M. Grujicic, B. Pandurangan, R. Qiao, B. A. Cheeseman, W. N. Roy, R. R. Skaggs, and R. Gupta, "Parameterization of the porous-material model for sand with different levels of water saturation," *Soil Dynamics and Earthquake Engng.*, **28**: 20-35 (2008).
28. V. S. Deshpande, R. M. McMeeking, H. N. G. Wadley, and A. G. Evans, "Constitutive model for predicting interactions between soil ejecta and structural panels," *J. Mech. Phys. Solids*, **57**(8): 1139-1164 (2009).
29. G. I. Kerely, "Numerical modeling of buried mine explosions," ARL-CR-461, Aberdeen Proving Ground, MD (2001).
30. W. Herrmann, "Constitutive equation for the dynamic compaction of ductile porous materials," *J. Appl. Phys.*, **40**(6): 2490-2499 (1969).

31. N. Gniazdowski, F. Gregory, A. D. Gupta, and P. W. Kingman, "Techniques for landmine-structure integration modeling," ARL-TR-2376, Army Research Laboratory, Aberdeen Proving Ground, MD, Jan. (2001).
32. A. D. Gupta, "Modeling and analysis of a 3-D asymmetric mine-soil-structure interaction problem with mine buried in dry sand," *71<sup>st</sup> Shock & Vibration Symp Proc.*, SAMAC, Falls Church, VA, Nov (2000).
33. G. I. Kerley, "The effects of soil type on numerical simulations of buried mine explosions," Report KTS02-3, Kerley Technical Services, Appomattox, VA (2002).
34. J. M. McGlaun, S. L. Thompson, and M. G. Elrick, "CTH: a three-dimensional shock wave physics code," *Int. J. Impact Engng.*, **10**: 351-360 (1990).
35. B. van Leer, "Towards the ultimate conservative difference scheme II: monotonicity of conservation combined in a second-order scheme," *J. Comp. Phys.*, **14**: 361-370 (1974).
36. B. van Leer, "Towards the ultimate conservative difference scheme IV: A new approach to numerical convection," *J. Comp. Phys.*, **23**: 276-299 (1977).
37. W. W. Predebon, C. E. Anderson Jr., and J. D. Walker, "Inclusion of evolutionary damage measures in Eulerian wavecodes," *Comp. Mech.*, **7**(4): 221-236 (1991).
38. A. Silling, "Stability and accuracy of differencing methods for viscoplastic models in wavecodes," *J. Comp. Phys.*, **104**: 30-40 (1993).
39. G. R. Johnson and W. H. Cook, "A constitutive model and data for metals subjected to large strains, high strain rates and high temperatures," *Proc. 7th Int. Symp. Ballistics*, pp. 541-548, The Hague, The Netherlands, 19-23 April (1983).
40. D. L. Littlefield and C. E. Anderson, Jr., "A study of zoning requirements for 2-D and 3-D long-rod penetration," *Shock Compression of Condensed Matter—1995* (S. C. Schmidt and W. C. Tao, Eds.), pp. 1135-1138, AIP Press, Woodbury, NY (1996).
41. R. B. Bird, W. E. Stewart, and E. N. Lightfoot, *Transport Phenomena*, John Wiley & Sons, NY, NY (1960).
42. C. E. Anderson, Jr., "An overview of the theory of hydrocodes," *Int. J. Impact Engng.*, **5**(1-4): 33-59 (1986).
43. W. E. Johnson and C. E. Anderson, Jr., "History and application of hydrocodes in hypervelocity impact," *Int. J. Impact Engng.*, **5**(1-4): 423-439 (1986).

UNCLASSIFIED

UNCLASSIFIED